

Spatial-scale dependence of aerosol indirect effects over land in eastern China: A comparative analysis

Yuqin Liu^{1,2}, Tao Lin^{1,2}, Jiahua Zhang³, Fu Wang⁴, Meixia Lin^{1,2}, Yuan Chen^{1,2}, Yiyi Huang^{1,2}, Hongkai Geng^{1,2}, Xin Cao^{1,2}, Gerrit de Leeuw^{5,6}

1 State Key Laboratory of Regional and Urban Ecology, Institute of Urban Environment, Chinese Academy of Sciences, Xiamen 361021, China

2 Fujian Key Laboratory of Digital Technology for Territorial Space Analysis and Simulation, Fuzhou 350108, China

3 Key Laboratory of Digital Earth Sciences, The Aerospace Information Research Institute, Chinese Academy of Sciences, Beijing 100094, China

4 CMA Earth System Modeling and Prediction Centre (CEMC), Beijing 100081, China

5 Royal Netherlands Meteorological Institute (KNMI), R&D Satellite Observations, 3730AE De Bilt, The Netherlands

6 State Key Laboratory of Remote Sensing and Digital Earth & Key Laboratory of Satellite Remote Sensing of Ministry of Ecology and Environment, Aerospace Information Research Institute, Chinese Academy of Sciences, Beijing 100101, China

Correspondence to: Tao Lin (tlin@iue.ac.cn); Gerrit de Leeuw (gerrit.de.leeuw@knmi.nl, ORCID: 0000-0002-1649-6333)

Abstract

This study aims to reveal patterns of the sensitivity of aerosol indirect effects to spatial scales and investigate the regulatory role of the liquid water path (LWP) in aerosol-cloud interactions over land in eastern China. Using MODIS and CALIOP satellite observations, we systematically analyzed the relationships between aerosol optical depth (AOD) and cloud properties (cloud droplet effective radius, CER; cloud droplet number concentration, N_d) during two periods: 2008–2014 (period 1, high AOD) and 2015–2022 (period 2, decreasing AOD). The results show two distinct regimes of CER variation with LWP: a rapid growth regime ($LWP < 55/50 \text{ g/m}^2$) and a decreasing regime ($LWP = 55-135/50-100 \text{ g/m}^2$) (thresholds vary by period). The sensitivity of CER to AOD (S_{CER}) exhibited a negative correlation, with stronger sensitivity in the decreasing LWP regime than in the rapid growth regime. Spatial scale (characterized by buffer size and study area) significantly modulated these sensitivities: $|S_{CER}|$ and the positive sensitivity of N_d to AOD (S_{N_d}) both decreased with increasing spatial scale. Optimal buffer sizes range from $6^\circ \times 6^\circ$ to $10^\circ \times 10^\circ$: increasing with study area in period 2 but decreasing in period 1 for the

34 decreasing LWP regime. Compared with period 1, $|S_{CER}|$ in period 2 significantly reduced, reflecting the
35 weakened aerosol-cloud interactions due to declining aerosol concentrations. Additionally, the optimal
36 buffer sizes for S_{Nd} are larger in the $8^\circ \times 8^\circ$ and $10^\circ \times 10^\circ$ study areas than in $4^\circ \times 4^\circ$ and $6^\circ \times 6^\circ$ areas. This
37 study reveals the scale-dependence of aerosol-cloud interactions, providing critical observational support
38 for optimizing climate model parameterization schemes.

39 **Keywords:** Aerosol, Cloud, Liquid water path, Scale effect, Satellite, Eastern China

40

41 1 Introduction

42 Aerosol particles, depending on their chemical composition and size, can serve as cloud condensation
43 nuclei (CCN) in liquid clouds or as ice nucleating particles (INP) in ice clouds. When CCN are activated,
44 they can alter the microphysical properties of clouds and affect precipitation, indirectly impacting the
45 Earth's radiative budget through aerosol-cloud interactions (aci) (Tao et al., 2012; Fan et al., 2016;
46 Rosenfeld et al., 2019; Rao and Dey, 2020; Bellouin et al., 2020; Dagan et al., 2023). An increase in CCN
47 concentrations results in a larger number of cloud droplets (N_d), and if the cloud liquid water path (LWP)
48 remains constant, it leads to a reduction in the cloud droplet effective radius (CER) (Twomey, 1974;
49 Feingold et al., 2003). The reduced CER leads to an increased reflection of solar radiation, i.e. a higher
50 cloud albedo, and enhances radiative forcing due to aerosol-cloud interaction (RFaci). The impact of
51 increasing aerosol particle numbers on cloud properties, while maintaining a constant LWP, is commonly
52 known as the "Twomey" effect (Twomey, 1977; Feingold, et al., 2001; Matheson et al., 2005; Koren et
53 al., 2005; Meskhidze and Nenes, 2010; Costantino et al., 2010; 2013). Another aspect of RFaci involves
54 quick adjustments, which could also cause changes in other cloud characteristics due to the rise in N_d and
55 the decrease of CER. For example, this may lead to a reduction in precipitation efficiency, causing an
56 increase in the LWP and cloud cover. As a result, the reflection of solar radiation is intensified (Albrecht,
57 1989). These two effects of aci are often categorized as the cloud albedo effect and the cloud lifetime
58 effect (Quaas et al., 2008).

59 Extensive research on the impact of aerosols on the microphysical properties of clouds has been
60 conducted utilizing satellite observations (Liu et al., 2017; Jia et al., 2022), aircraft measurements (Jia et
61 al., 2019; Zheng et al., 2024), ground-based monitoring (Sarna et al., 2016; Zheng et al., 2020), and
62 numerical simulations (Lee et al., 2025; Li et al., 2008). Among these, satellite-based instruments have

63 become a vital observational tool for studying aerosol-cloud interactions due to their wide spatial
64 coverage and high spatiotemporal resolution. However, optical satellite sensors such as the Moderate
65 Resolution Imaging Spectroradiometer (MODIS) cannot effectively penetrate cloud layers (King et al.,
66 2003; Kaufman et al., 2005; Remer et al., 2005), making it difficult to directly retrieve the optical
67 properties of aerosols underneath clouds. Currently, aerosol data are mainly obtained in cloud-free
68 conditions as determined using cloud detection methods. This limitation results in significant spatial
69 mismatches between aerosol and cloud properties, often requiring aggregation of satellite data over large-
70 scale grids for statistical analysis to determine relationships between aerosol and cloud parameters. The
71 discrepancy between this large-scale analysis and the actual process scale frequently leads to biases in
72 quantifying aerosol indirect effects, thereby significantly increasing the uncertainty in radiative forcing
73 estimates (Lebsock et al., 2013; Altaratz et al., 2014; Ma et al., 2015; Possner et al., 2016; Bender et al.,
74 2018).

75 In recent years, studies based on multi-source satellite data or multi-instrument joint observations have
76 demonstrated that aerosol particles significantly influence cloud microphysical properties (Saponaro et
77 al., 2017; Liu et al., 2018; Pandey et al., 2020). Numerous studies have validated the existence of the
78 Twomey effect (Jones et al., 2009; Christensen et al., 2016; Jia et al., 2019). However, also studies have
79 been published with findings that contradict the Twomey effect, particularly over land, where an increase
80 in aerosol optical depth (AOD) results in an increase in CER (Feingold et al., 2001; Yuan et al., 2008;
81 Grandey and Stier, 2010; Tang et al., 2014; Wang et al., 2015; Ma et al., 2018; Jia et al., 2019; Liu et al.,
82 2020). These inconsistent findings highlight the complexity and regional variability of aci mechanisms,
83 and further in-depth research is needed to reveal the underlying processes.

84 Currently, researchers usually use grid methods (such as $1^\circ \times 1^\circ$, $2^\circ \times 2^\circ$, etc.) to study the aerosol indirect
85 effects in large areas (Bréon, 2002; Kaufman et al., 2005; Bulgin et al., 2008; Quaas et al., 2008). For
86 instance, Grandey and Stier (2010) estimated the relationship between aerosols and CER on a global
87 scale ($60^\circ\text{N}\sim 60^\circ\text{S}$) using multiple spatial resolutions ($1^\circ \times 1^\circ$, $4^\circ \times 4^\circ$, $8^\circ \times 8^\circ$, $15^\circ \times 15^\circ$, and $60^\circ \times 60^\circ$). They
88 concluded that the sensitivity of retrieved CER to AOD generally exhibited positive values over land and
89 negative values over oceans, and pointed out that using grids larger than $4^\circ \times 4^\circ$ could introduce significant
90 errors due to the spatial variability of aerosol and cloud parameters. Additionally, the study highlighted
91 that, when using grids larger than $4^\circ \times 4^\circ$ to investigate the relationship between aerosols and CER,

92 significant errors could be introduced in calculating the aerosol indirect effect index due to the spatial
93 variability of aerosol and cloud parameters.

94 For studies focusing on smaller regions, researchers often employ a moving window or a fixed area
95 referred to as a buffer zone, within which the distribution of aerosol concentrations is assumed to be
96 uniform. Spatially matched samples are constructed by averaging AOD and cloud parameters within the
97 window or buffer zone. The choice of the window or buffer size is often arbitrary, and existing studies
98 rarely systematically explore how the detection of aci signals is influenced by the size of the area. For
99 example, Yuan et al. (2008) used a 100 km × 100 km moving window to calculate the mean values of
100 AOD and cloud properties to investigate the relationship between aerosols and CER across seven global
101 regions. Their results indicated that only two of these regions, near the coasts of the Gulf of Mexico and
102 the South China Sea, exhibited a positive correlation between CER and AOD. Similarly, Jones et al.
103 (2009) utilized multi-source remote sensing data and applied a point spread function to derive the mean
104 AOD within a 20 km range, which was designed to match the native 20 km resolution of the
105 corresponding cloud properties (cloud optical thickness, COT; LWP; CER; cloud top pressure, CTP).

106 Their study examined the influence of aerosol types, cloud conditions, and atmospheric factors on aerosol
107 indirect effects across six different oceanic regions globally, finding that the sensitivity of cloud
108 properties to AOD varied substantially with regional characteristics. In addition, significant progress has
109 been made in research utilizing observations from the Cloud-Aerosol Lidar with Orthogonal Polarization
110 (CALIOP) data (Winker et al., 2007). For instance, Costantino et al. (2010) used CALIOP data to
111 investigate the aerosol influence on CER in stratocumulus clouds over the coastal regions of Namibia
112 and Angola. They performed the analysis by co-locating an aerosol index (based on AOD and the
113 Ångström exponent) with CER within a 150 km buffer zone around CALIOP observations. They found
114 that there was no correlation between aerosol load and CER when aerosol and cloud layers were clearly
115 separated, but a strong correlation when lidar profiles indicated mixing. Costantino et al. (2013) further
116 analyzed the statistical relationship between aerosol concentrations and cloud physical parameters by
117 examining aerosol and cloud properties within a 20 km buffer zone around CALIOP samples, integrating
118 vertical profiles of aerosol and cloud data. Their statistics also clearly showed that cloud micro-physical
119 properties were affected by aerosols when aerosol and cloud layers were mixed, decreasing the CER. It
120 is noted that these two studies by Costantino et al. (2010, 2013) reached consistent conclusions about aci

121 (i.e., aerosols modulate CER when layers interact), by adopting different buffer sizes (150 km vs. 20 km)
122 to target distinct study areas. This demonstrates that the buffer size is tailored to the research objectives
123 rather than through a systematic sensitivity analysis. Wang et al. (2015) revealed an inverse “Twomey”
124 effect between aerosols and CER in eastern China by analyzing aerosol concentrations and CER within
125 a 50 km buffer zone around CALIOP samples. Their results showed that larger CER was associated with
126 high AOD, which was attributed to the feedback of microphysical processes from intense competition
127 for vapor in the presence of high aerosol concentrations and the evaporation of smaller, less hygroscopic,
128 droplets. Similarly, Liu et al. (2017) systematically examined the response mechanisms of warm cloud
129 macro- and microphysical parameters to increasing AOD in the Yangtze River Delta region, also using
130 CALIOP samples within a 50 km buffer zone. They found that the relation between cloud properties and
131 AOD depended on the aerosol abundance, with a different behavior for low and high AOD (i.e. $AOD <$
132 0.35 and $AOD > 0.35$). However, both Wang et al. (2015) and Liu et al. (2017) used a fixed 50 km buffer
133 zone without justifying the choice or exploring how varying buffer sizes might alter the strength or
134 robustness of their findings—a common limitation in regional aci studies. More recently, Liu et al. (2024)
135 quantified the relative importance of aerosols, meteorological parameters and their interactions for cloud
136 properties in the eastern coastal and inland regions of China, utilizing MODIS $1^\circ \times 1^\circ$ aerosol and cloud
137 product data. Their study confirmed that CER decreased with the increase in AOD in the moderately
138 polluted atmosphere ($0.1 < AOD < 0.3$) over the East China Sea, whereas, in contrast, CER increased
139 with increasing AOD in the polluted atmosphere ($AOD > 0.3$) over the Yangtze River Delta. These studies
140 have provided critical scientific insights into aci at regional scales, but the lack of systematic scale
141 sensitivity analysis—especially for varying window/buffer sizes within the same regional domain—
142 leaves uncertainties about the generalizability of their conclusions.
143 However, the properties and interaction processes of aerosols and clouds are spatially significantly
144 heterogeneous and scale dependent (McComiskey et al., 2009; McComiskey and Feingold, 2012; Chen
145 et al., 2015; Glotfelty et al., 2020). McComiskey and Feingold (2012) explicitly pointed out that the
146 “scale problem” is a major challenge in quantifying aerosol indirect effects, as the spatial scale of
147 observation can mask or exaggerate the true interaction signals. In previous studies, the definitions of
148 window size and buffer size have often been subjective, inadvertently introducing uncertainties into the
149 research on aci. Although studies have explored the relationship between aerosols and CER across

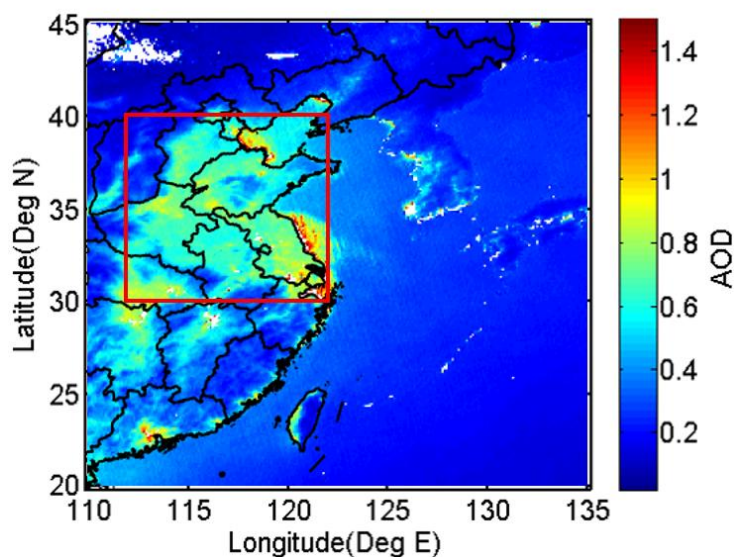
150 different observational scales, these investigations have primarily focused on larger spatial scales, leaving
151 a gap in sensitivity analysis of aerosol indirect effects at smaller regional scales. For example, Grandey
152 and Stier (2010) focused on global-scale grid resolutions but did not explore the scale dependence within
153 regional domains; Wang et al. (2015) and Liu et al. (2017) used fixed buffer sizes (50 km) without
154 investigating how varying buffer sizes affect the results. Therefore, utilizing multi-source remote sensing
155 data to explore whether and how the aerosol indirect effect depends on observational spatial scales in
156 eastern China is of great significance for developing parameterization schemes that align with the
157 regional characteristics of aci.

158 Aerosol properties in China have significantly changed between 2008 and 2022 due to economic
159 development and the implementation of emission reduction policies. The AOD over China increased
160 until 2007 to become among the highest worldwide and remained high between 2008 and 2014 with large
161 interannual variations. The enforcement of emission reduction measures, in particular the implementation
162 of the 2013-2017 Clean Air Action Plan, resulted in the decline of the AOD between 2014 and 2018 (de
163 Leeuw et al., 2021; 2022; 2023) and a further decrease resulted in an AOD lower than that in 2000 (de
164 Leeuw et al., 2023). This distinct two-period variation (high AOD vs. decreasing AOD) provides a unique
165 opportunity to investigate how changes in aerosol loading modulate the scale dependence of aerosol
166 indirect effects, a topic that has not been systematically addressed in previous studies. Based on these
167 observations, in this study we conduct a comparative analysis of the sensitivity of cloud parameters (CER
168 and N_d) to AOD variation using data from two distinct periods: 2008-2014 (period 1, high AOD) and
169 2015-2022 (period 2, decreasing AOD). The main objectives of this study are to: (1) reveal patterns of
170 the sensitivity of aerosol indirect effects to spatial scales by investigating how spatial scale modulates
171 the sensitivity of CER to AOD (S_{CER}) and the sensitivity of N_d to AOD (S_{N_d}) over eastern China during
172 the two periods; and (2) clarify the regulatory role of LWP in cloud-aerosol interaction by examining the
173 LWP-stratified responses of S_{CER} and S_{N_d} to spatial scale and AOD variations. The study aims to reveal
174 the patterns of the sensitivity of aerosol indirect effects to spatial scales, provides support for optimizing
175 parameterization schemes and accurate assessment of regional aerosol effects.

176 **2 Method**

177 **2.1 Study area**

178 Eastern China (30°N-40°N, 112°E-122°E; Figure 1) has undergone remarkable economic expansion over
179 the past three decades, which was accompanied by a substantial increase in AOD. Eastern China presents
180 a unique atmospheric laboratory due to its complex aerosol composition - featuring both anthropogenic
181 pollutants from industrial emissions and natural mineral dust transported from Central Asian deserts,
182 particularly during the spring (Proestakis et al., 2018; Liu et al., 2021). The multitude of sources and the
183 persistent nature of these aerosol particles, which can remain suspended for days to weeks and be
184 transported over long distances in the absence of precipitation (Costantino et al., 2013; Li et al., 2021;
185 Leung et al., 2023), makes eastern China an ideal study area for investigating aci. Our research leverages
186 satellite observations to systematically evaluate the sensitivity of cloud properties (S_{CER} and S_{Nd}) to the
187 AOD variation, thereby revealing the scale-sensitive patterns of aerosol indirect effects and clarifying
188 the regulatory role of LWP in cloud-aerosol interactions over this region.



189
190 **Figure 1.** Map of annual averaged MODIS/AQUA level 2 AOD for all years during the period from 2008 to
191 2022. The red rectangle (30°–40°N, 112°–122°E) indicates the study area.

192 **2.2 Data used**

193 Data used in this study were acquired by the MODIS instrument aboard NASA’s Aqua satellite, which
194 features an extensive swath width of approximately 2300 km and comprehensive spectral coverage across
195 multiple bands (King et al., 2003). The satellite’s equator crossing time is 13:30 (Local time, i.e. in the

196 early afternoon, coinciding with optimal development conditions for continental warm cloud systems
197 (Wang et al., 2014; Liu et al., 2024). For aerosol characterization, we utilized the MODIS Collection 6.1
198 aerosol product (MOD04), generated from cloud-screened pixels with a native resolution of 500 m at
199 nadir and subsequently aggregated to 10 km grid cells (Remer et al., 2005; Levy et al., 2010). AOD
200 retrieval over land uses radiances measured at the top of the atmosphere (TOA) at wavelengths of 0.47,
201 0.66, and 2.13 μm (Remer et al., 2005). The MODIS AOD (at 550 nm) Level 2 product (10 km \times 10
202 km) has been validated against ground-based remote sensing data and the results show that 69.40% of
203 the MODIS AOD data fall within the expected uncertainty of $\pm (0.05 + 15 \%)$ over land (Levy et al.,
204 2013). In this study, AOD larger than 1.5 was excluded from further analysis to mitigate potential
205 retrieval overestimation. This threshold was selected based on two key considerations: (1) Christensen
206 et al. (2017) used MOD06 C6 data (1 km \times 1 km) and reported that “large aerosol optical depths remain
207 in the MODIS-observed pixels near cloud edges, due primarily to 3D effects (Varnáí and Marshak, 2009)
208 and the swelling of aerosols by higher relative humidity”; (2) the threshold of 1.5 aligns with widely
209 adopted thresholds in regional aerosol-cloud interaction studies over eastern China, where high AOD
210 often coincides with complex surface conditions (e.g., urbanization, heterogeneous land cover) that
211 exacerbate retrieval biases (Wang et al., 2015; Liu et al., 2017, 2021).

212 The cloud properties used in this study, including CER, LWP, COT, CTP, and cloud phase infrared (CPI)
213 index, were derived from the Collection 6.1 MODIS Level 2 cloud product (MYD06) (King et al., 2003).
214 The retrieval of these cloud characteristics utilizes six spectral channels spanning wavelengths from the
215 visible to the near-infrared (0.66, 0.86, 1.24, 1.64, 2.12, and 3.75 μm) as described by King et al. (1997).
216 Uncertainties in the MODIS C6.1 cloud parameters over land originate from instrument calibration,
217 atmospheric correction, land surface properties, and model assumptions (Platnick et al., 2017, 2018). For
218 COT, these include scene-dependent Level 1B data errors (1.5%–30%), land surface albedo errors
219 ($\pm 15\%$), and atmospheric correction errors ($\pm 20\%$). The C6.1 algorithm addresses some prior limitations
220 by inheriting C6’s optimized lookup table design, which reduces interpolation errors to 0.1%–0.2% for
221 near-nadir views and corrects C5’s overestimation of thin-cloud COT (Platnick et al., 2017). CER
222 uncertainties, stemming from solar irradiance error ($\sim 4\%$ at 3.7 μm), atmospheric correction, and
223 scattering differences, are mitigated as C6.1 retains C6’s separate multi-band reporting, thereby
224 eliminating C5’s systematic bias (Platnick et al., 2017). LWP uncertainty is linked to COT/CER retrieval

225 errors and cloud-phase classification accuracy; the latter is improved by C6's voting-based phase
226 algorithm (preserved in C6.1), which reduces misclassification over complex surfaces like vegetation
227 and deserts (Marchant et al., 2015; Platnick et al., 2017). For CTP (1 km resolution), uncertainties from
228 viewing angles and cloud structure are partially countered in C6.1 by assigning fill values when the 1 km
229 retrieval fails, avoiding surface parameter defaults. For land clouds above 3 km, CTP accuracy reaches
230 ~50 hPa (Baum et al., 2012). Finally, CPI adopts C6's weighted voting logic (replacing C5's sequential
231 tree), with C6.1 maintaining an enhanced Phase Agreement Fraction against CALIOP/POLDER data,
232 which reduces uncertainties from weak thin-cloud signals and complex land interference (Marchant et
233 al., 2015; Platnick et al., 2017).

234 Following the methodology of Platnick et al. (2017), CER and COT measurements at $3.7 \mu\text{m}$ were used
235 to estimate N_d through adiabatic approximation principles (Quaas et al., 2006). Previous investigations
236 have demonstrated that implementing filters based on cloud adiabaticity produced minimal effects on
237 S_{Nd} estimates while significantly reducing the available dataset by up to 63.00% (Gryspeerd et al., 2022).
238 Therefore, such filtering procedures were not adopted in the current analysis. Instead, N_d calculations are
239 initially performed at the native pixel resolution (approximately 1 km) prior to spatial aggregation,
240 thereby avoiding potential biases associated with deriving N_d from nonlinear combinations of CER and
241 COT at coarser resolutions (Feingold et al., 2022). To maintain data quality, the analysis incorporated
242 several quality control measures: only single-phase liquid clouds (CPI = 1) with CTP exceeding 700 hPa
243 and LWP smaller than 200 g m^{-2} are considered, consistent with the typical atmospheric distribution of
244 aerosols in the lower troposphere (Michibata et al., 2014). Pixels with CER values smaller than $4 \mu\text{m}$ or
245 COT values smaller than 4 were excluded due to increased retrieval uncertainties (Sourdeval et al., 2016).
246 Additionally, observations were restricted to solar zenith angles $<65.00^\circ$ and sensor zenith angles
247 $<41.40^\circ$. This constraint was intended to reduce the influence of well-documented biases, as elaborated
248 in Grosvenor et al. (2018).

249 CALIPSO (Cloud-Aerosol Lidar and Infrared Pathfinder Satellite Observations) operates within the A-
250 Train constellation alongside the Aqua satellite and other NASA Earth-observing platforms. The primary
251 instrument aboard CALIPSO is the Cloud-Aerosol Lidar with Orthogonal Polarization (CALIOP).
252 CALIOP is a two-wavelength, polarization-sensitive lidar specifically designed to provide high-
253 resolution vertical profiles of aerosols and clouds on a global scale (Winker et al., 2009). The mission

254 and its lidar instrument are described in Winker et al. (2009), and the associated Level 1 data products
255 are detailed in Winker et al. (2010). This advanced sensor features an exceptionally narrow ground
256 footprint of 70 m diameter for each laser pulse. The vertical resolution of CALIOP's products varies with
257 altitude: 30 m within 0-8.2 km, 60 m between 8.2-20.2 km, and 180 m from 20.2-30.1 km, while
258 maintaining a consistent 5 km horizontal resolution along the track direction (Liu et al., 2009).
259 The coordinated A-Train configuration ensures near-simultaneous observations (within 1-2 minutes)
260 between MODIS/Aqua and CALIOP/CALIPSO for identical atmospheric targets (Stephens et al., 2002).
261 This temporal synchronization guarantees data consistency when extracting coincident measurements,
262 avoiding interferences such as aerosol diffusion and cloud evolution caused by observational time lags—
263 an advantage unparalleled by positioning methods like random grid points and ground-based stations.
264 For spatial compatibility, we resampled the higher-resolution MODIS cloud products (CER, LWP, and
265 N_d at 1 km native resolution) to match CALIOP's 5 km along-track scale, while directly utilizing the 5
266 km-resolution CTP and CPI parameters. In cases where CALIOP detected aerosol presence, we
267 computed spatial averages of MODIS aerosol and cloud retrieval products across multiple observation
268 scales (detailed in Section 2.4) centred on CALIOP targets. This approach assumes reasonable
269 homogeneity of aerosol properties between adjacent clear and cloudy regions (Anderson et al., 2003;
270 Quaas et al., 2008). Table 1 provides a comprehensive overview of the aerosol and cloud datasets
271 including the parameters used from each product, the resolution, and the data source, used in this study.

272
273
274
275
276
277
278
279
280
281
282
283

284 **Table 1. Aerosol and cloud products, parameters, horizontal resolutions, and their sources applied in the**
 285 **present study.**

Product	Parameters	Horizontal resolution	Data source		
Aerosol (MYD04 Level 2 Collection 6)	Latitude	10 km	MODIS		
	Longitude	10 km			
	Scan_Start_Time	10 km			
	AOD at 550 nm	10 km			
Cloud (MYD06 Level 2 Collection 6)	Latitude	5 km			
	Longitude	5 km			
	Scan_Start_Time	5 km			
	CER at 3.7 um and 2.1 um	1 km			
	LWP at 3.7 um	1 km			
	COT at 3.7 um	1 km			
	Cloud multi-layer flag	1 km			
	Cloud_Phase_Infrared_Day	5 km			
	Cloud_TOP_Pressure_Day	5 km			
	Sensor_Zenith_Day	5 km			
	Solar_Zenith_Day	5 km			
	Aerosol (05kmALay)	Latitude		5 km	CALIOP
		Longitude		5 km	
Profile_Time		5 km			

286 **2.3 Calculation of sensitivities**

287 Variations in aerosol loading significantly influence cloud optical properties (such as COT) and
 288 microphysical parameters (such as CER). Under specific environmental conditions, aerosol particles can
 289 transform into CCN or INP, a process primarily determined by their chemical composition and ambient
 290 temperature (Bellouin et al., 2020). When these nuclei are activated, water vapor condenses on their
 291 surfaces to form cloud droplets or ice particles. As the concentration of aerosol particles increases, the
 292 number of CCN or INP may rise correspondingly, leading to an increase in the number of cloud droplets.
 293 Notably, under conditions where the liquid water content in clouds remains constant (i.e., LWP), the same
 294 amount of water vapor is distributed across more cloud droplets, resulting in a reduction in the size of
 295 individual droplets. Specifically, as aerosol concentration increases, the CER decreases, while cloud
 296 albedo increases. On the basis of findings of Kaufman and Fraser (1997), Feingold et al. (2001) pointed
 297 out that the sensitivity of cloud microphysical properties (e.g., CER) to changes in the number
 298 concentration of aerosol particles (e.g., using AOD as a measure) can be described by the following
 299 formula:

300
$$S_{\text{CER}} = \left. \frac{d \ln r_e}{d \ln \alpha} \right|_{\text{LWP}} \quad -0.33 < S < 0 \quad (1)$$

301 Where r_e represents the CER and α represents the AOD. Following Andreae (2009), AOD and CCN
 302 are correlated and AOD varies with CCN following a power law relationship. Eq. (1) describes the
 303 relative change of CER with the relative change of the AOD for constant LWP. It is noted that this
 304 formulation differs from that used in recent studies (e.g., Bellouin et al., 2020) where S is expressed in
 305 terms of N_d with no restriction in LWP. The sensitivity S of CER to AOD can be determined as the slope
 306 of a linear fit to a log-log plot of CER versus AOD. The effect of aerosols on CER is analyzed by
 307 comparing the difference in S_{CER} and correlation coefficients between AOD and CER under different
 308 spatial scales (Section 2.4) and LWPs (Section 3.2).

309 In this study, the variation in N_d with CCN is referred to as the susceptibility S_{N_d} . Following the method
 310 of Gryspeerdt et al. (2023), the sensitivity, S_{N_d} , of a cloud property, N_d , to α is defined here as

311
$$S_{N_d} = d \ln N_d / d \ln \alpha \quad 0 < S < 1 \quad (2)$$

312 Relations between CER and N_d and AOD are determined through Eq. 1 and Eq. 2 and correlation
 313 coefficients R. The significance of these relations is determined by using the student's t test, i.e. the
 314 results are statistically significant when the p value is smaller than 0.01, where p is defined as the
 315 probability of obtaining a result equal to or "more extreme" than what was actually observed.

316 This method quantifies the sensitivity of CER and N_d to AOD variations via linear regression in log-log
 317 space, using Eq. 1 and Eq. 2, respectively. Its core assumptions, uncertainties, and limitations are highly
 318 consistent: both rely on AOD as an aerosol proxy variable, assume constant cloud liquid water content
 319 and a linear sensitivity relationship, and depend on the reliability of satellite-retrieved parameters
 320 (Feingold et al., 2001; Gryspeerdt et al., 2023). However, AOD cannot distinguish aerosol size and
 321 hygroscopicity, retrieval errors are substantial in clean conditions, and linear fitting fails to capture
 322 nonlinear/non-monotonic responses. Both methods are constrained by satellite retrieval biases, limited
 323 scenario applicability (only valid for specific homogeneous clouds and aerosol types), the omission of
 324 key modulating factors (dynamical conditions, aerosol type) and feedback processes, and can only assess
 325 first-order direct effects. Reliability requires scenario constraints and uncertainty analysis; the only
 326 nuances come from the target variable (CER vs. N_d), which do not alter the shared methodological
 327 limitations.

328

329 2.4 Research design for scale effects analysis

330 This study was conducted at multiple spatial scales to examine the scale dependence of S_{CER} and S_{Nd} in
331 delineating aci (Fig. 2). Here, the spatial scales are described by two parameters: study area size (the
332 geographic scope of the analysis) and buffer size (the local spatial extent around each observation point
333 for aggregating aerosol and cloud data). To this end, the study area was divided into four congruent square
334 research areas all centered at the same geographical location (35°N, 117°E) over Eastern China. Hence,
335 spatial extent varies from the whole study area as defined in Section 2.1 (30°N-40°N, 112°E-122°E) to
336 successively smaller areas simulated by decreasing the study area in steps of 2° to 4°×4° as illustrated in
337 Figure 2a.

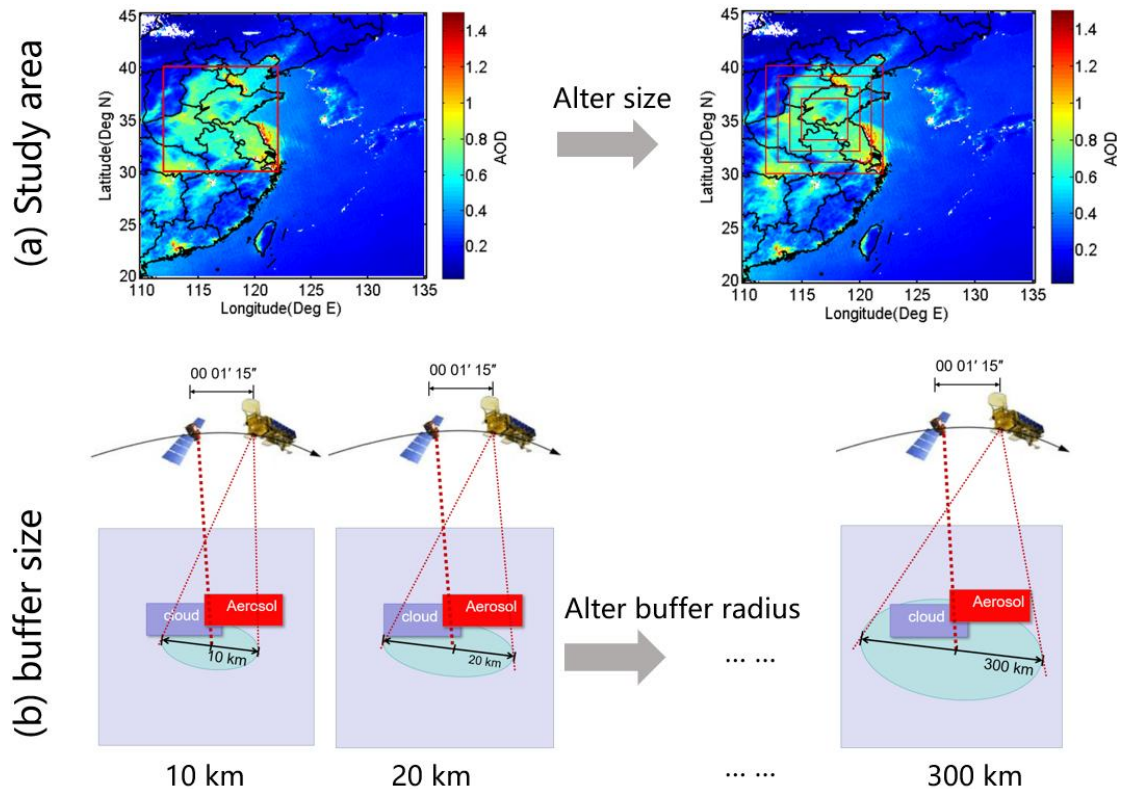
338 Buffer size refers here to a circular spatial domain centered at each CALIOP-detected point in the study
339 area where CALIOP detected the presence of aerosols. Within this circular domain, MODIS-retrieved
340 cloud and aerosol data (AOD, CER, N_d , LWP) are spatially averaged to construct matched aerosol-cloud
341 datasets at different local scales. As previously noted, this approach relies on the assumption that aerosol
342 properties are reasonably homogeneous between adjacent clear and cloudy regions (Anderson et al., 2003;
343 Quaas et al., 2008), and this premise is supported by the short-range transport of aerosols (e.g., 10–300
344 km) and the near-simultaneous observations (1–2 minutes) by MODIS and CALIOP within the A-Train
345 constellation.

346 Buffer zones with sizes increasing from 10 to 300 km (10 km, 20 km, 30 km, 40 km, 50 km, 60 km, 70
347 km, 80 km, 90 km, 100 km, 120 km, 140 km, 150 km, 160 km, 180 km, 200 km, 250 km, and 300 km)
348 were determined within the whole study area by using CALIOP data. Previous observations indicate that
349 the typical horizontal scale of cloud clusters ranges from tens to hundreds of kilometers (Zhang et al.,
350 2024; Cai et al., 2022), supported by CloudSat/CALIPSO satellite data showing power-law distributed
351 cloud scales (10-1000 km fitting range) covering major cloud types (Zhang et al., 2024) and regional
352 evidence of consistent multi-season, multi-latitude cloud extents (Cai et al., 2022). Meanwhile, aerosol
353 spatial homogeneity varies with distance: local-scale aerosols (≤ 50 km) exhibit high homogeneity due
354 to consistent sources and stable diffusion, while regional-scale aerosols (> 100 km) show enhanced
355 heterogeneity from multi-source mixing and atmospheric transport (Hassan et al., 2024; Mohebalhojeh
356 et al., 2026). Thus, the 10–300 km buffer range covers both cloud characteristic scales and the aerosol
357 homogeneity transition range, ensuring that MODIS data averaging effectively captures cloud-aerosol

358 coupling. This range avoids insufficient MODIS pixel coverage due to excessively small buffer sizes (<
359 10 km). It also prevents conflation between regional meteorological variations and local aci signals
360 arising from overly large buffer sizes (> 300 km), as synoptic-scale circulation and other regional
361 meteorological changes may interfere with local aci signals (Quaas et al., 2010). Meanwhile, this range
362 aligns with the 50 - 150 km buffer sizes widely adopted in regional aci studies (Wang et al., 2015; Liu et
363 al., 2017; 2024), enabling cross-validation of results and ensuring that MODIS data averaging effectively
364 captures cloud-aerosol coupling.

365 MODIS-retrieved cloud and aerosol data were averaged over a buffer area around each CALIOP data
366 point with a radius varying from 10 km to 300 km. Thus, a dataset including aerosol and cloud properties
367 was constructed with different buffer sizes. The effect of buffer size on the sensitivity of CER and N_d to
368 variations in AOD was determined in each study area varying from $4^\circ \times 4^\circ$ to $10^\circ \times 10^\circ$. To this end, for
369 each buffer size, the averaged AOD and cloud parameters were paired to calculate the sensitivities S_{CER}
370 (Eq. 1) and S_{N_d} (Eq. 2), as well as their correlation coefficients (R) between cloud properties (e.g., CER,
371 N_d) and AOD. The optimal buffer size for each study area is defined as the one maximizing the R. This
372 definition is adopted based on two core considerations. Firstly, it aligns with the statistical principle that
373 a higher R value indicates a stronger linear correlation between the two variables in the log-log space,
374 minimizing the interference of random noise and non-aerosol confounding factors on the sensitivity
375 estimation (Quaas et al., 2006; Gryspeerd et al., 2022). This ensures that the derived S_{CER} can reliably
376 reflect the intrinsic relationship between aerosol loading and cloud droplet effective radius, rather than
377 spurious correlations caused by inappropriate spatial scales. Secondly, this definition also facilitates
378 comparability with existing literature, as it aligns with the methodological framework of satellite-based
379 aerosol-cloud interaction studies (Saponaro et al., 2017; Liu et al., 2021). In these studies, the optimal
380 spatial scale is typically identified by maximizing the statistical robustness of variable correlations.

381 The dataset was used to study the characteristics of aerosol indirect effects as function of buffer size and
382 study area, for two different periods: one with a high aerosol content (2008-2014) and another one with
383 a decreasing aerosol content (2015-2022). This approach enabled the determination of the optimal buffer
384 size for aerosol indirect effects as function of the size of the study area, ultimately leading to the
385 development of a parameterization scheme for aerosol indirect effects for observations with different
386 spatial resolution and different sizes of the study area over eastern China.



387

388 **Figure 2. (a) Schematic diagram of study area and buffer size patterns applied in this study. (b) scheme of**
 389 **CALIPSO-MODIS coincidence methodology. When CALIPSO detects the presence of aerosol and cloud fields,**
 390 **we look for MODIS retrievals within a buffer size from the CALIPSO target. The temporal coincidence is**
 391 **insured by the coordinated satellite orbits.**

392 3 Results

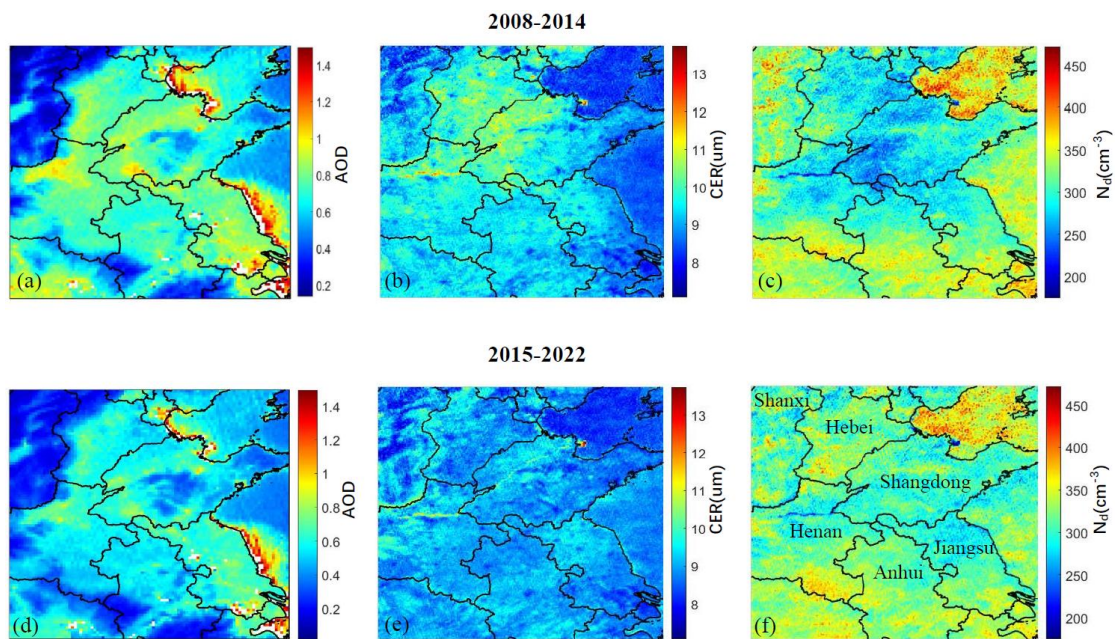
393 3.1 Spatial variations of aerosol and cloud parameters

394 Figure 3 illustrates the spatial distributions of AOD and cloud properties (CER and N_d) across the study
 395 region, averaged for the periods 2008-2014 and 2015-2022. The AOD spatial patterns (Fig. 3a,d) show
 396 similar spatial distributions during both periods, but with notably reduced values during the latter.
 397 Pronounced spatial gradients in AOD are evident during both periods. The lowest AOD values occur over
 398 the mountainous regions of Shanxi province in the northwest, while elevated concentrations appear in
 399 the southeastern areas encompassing the Hebei and Shandong provinces. This geographical contrast
 400 arises from the mountain ranges that demarcate the heavily industrialized, densely populated North China
 401 Plain (NCP) in the east - characterized by substantial anthropogenic emissions - from the relatively
 402 pristine western regions. Under prevailing southeasterly wind conditions, these topographic barriers
 403 effectively block transport of atmospheric pollutants which accumulate along their windward slopes

404 (Sundström et al., 2012). The concentration of heavy industries and power generation facilities in the
 405 NCP are primarily responsible for the observed high AOD concentrations, together with meteorological
 406 and geographical conditions. Additionally, lower AOD values appear in southern Anhui and central
 407 Shandong relative to the surrounding regions.

408 The CER spatial distributions (Fig. 3b,e) reveal distinct differences between the two periods. During
 409 2008-2014, larger cloud droplets predominated in the northern sectors, particularly throughout Hebei and
 410 western Shandong. Notably, the spatial correspondence between AOD and CER maxima aligns with the
 411 anti-Twomey effect, suggesting that the high aerosol loading promoted cloud droplet growth rather than
 412 suppression - consistent with findings from Wang et al. (2014) and Liu et al. (2018). The 2015-2022
 413 period shows markedly reduced CER values (typically $<10 \mu\text{m}$) with enhanced spatial homogeneity.

414 Similarly, N_d exhibits contrasting spatial patterns between the two periods (Fig. 3c,f). The earlier
 415 timeframe shows depressed N_d values in central regions surrounded by elevated concentrations
 416 peripherally. This pattern reverses during 2015-2022, with increases of N_d in the central area
 417 accompanied by overall reduction of the cloud droplet concentrations in the surrounding regions.

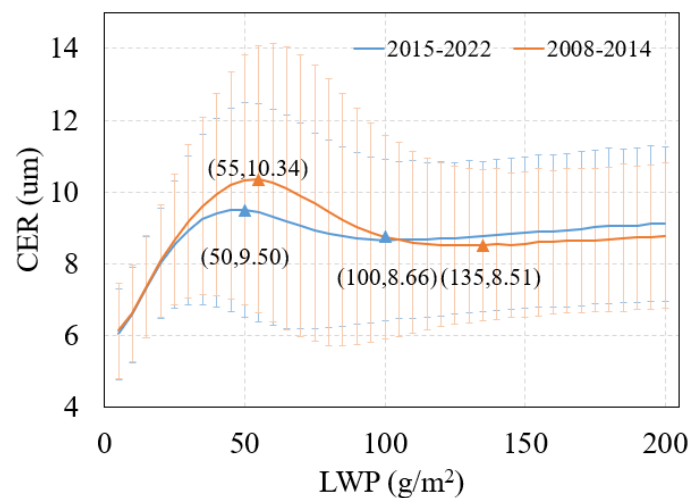


418
 419 **Figure 3. Spatial distributions of AOD (a, d), CER (b, e) and N_d (c, f), averaged over the years 2008-2014 (top**
 420 **row) and 2015-2022 (bottom row) over the study area. The lines are provincial borders and the names of**
 421 **provinces mentioned in the text are indicated in Fig. (f).**

422 3.2 Sensitivity of CER to AOD stratified by LWP

423 Before analyzing the influence of AOD on CER, the relationship between CER and LWP should be

424 investigated. The values of the LWP were divided into 40 subsets with a width of 5 g/m^2 , and then the
 425 average value of CER in each subset was calculated and plotted as function of LWP (Figure 4).
 426 The variation of CER with LWP shows three regimes. For LWP smaller than 55 g/m^2 (period 1) or 50
 427 g/m^2 (period 2), CER increased rapidly with the increase of LWP. This first LWP regime is referred to as
 428 a rapid growth regime (LWP1). The second LWP regime, referred to as a decreasing regime (LWP2),
 429 applies to the LWP range from 55 g/m^2 to 135 g/m^2 (period 1) or $50\text{-}100 \text{ g/m}^2$ (period 2) and CER
 430 decreased with the increase of LWP. When LWP was greater than 135 g/m^2 (period 1) or 100 g/m^2 (period
 431 2), CER increased with increasing LWP but at a much slower rate than during the first regime; the third
 432 LWP regime is therefore referred to as a slow growth regime (LWP3). These results show that CER is
 433 very sensitive to the changes in LWP, which is consistent with the study of Liu et al. (2021). Specifically,
 434 CER exhibited a three-stage variation with LWP: rapid growth when $\text{LWP} < 50 \text{ g/m}^2$ (with the fastest
 435 change rate), a stable state during $50\text{-}150 \text{ g/m}^2$, and slow growth when $\text{LWP} > 150 \text{ g/m}^2$ (at a rate much
 436 lower than the first stage). This highlighted the necessity of fixing LWP conditions to accurately
 437 investigate the impact of AOD on CER. To separate the effects of changing LWP on CER from those of
 438 changing AOD on CER, relations between CER and AOD were evaluated for constant LWP
 439 (McComiskey et al., 2012), for each of the three regimes mentioned above, by using double-logarithmic
 440 plots of AOD versus CER. The number of CER observations in the third regime is too small to achieve
 441 statistically meaningful results, therefore the sensitivity of CER to AOD was only analyzed for the rapid
 442 growth and decreasing regimes.



443
 444 **Figure 4. Variation of CER with LWP over the study area. Here all CER data were averaged in LWP bins,**
 445 **from 0 to 200 g/m^2 with a width of 5 g/m^2 . The red line is a fit to the data during 2008-2014 and the blue line**
 446 **for the data during 2015-2022. The numbers in parentheses indicate the (LWP, CER) values for the inflection**

447 points between the regimes. The error bars (the vertical lines) denote the standard deviations, indicating the
448 variability of CER around the average at each LWP value.

449 3.2.1 Rapid CER growth regime

450 For the first LWP regime, the S_{CER} is negative (as shown in Figure 5). This aligns with the Twomey effect
451 (Twomey, 1977): an increase in aerosols raises the number of CCN, and with constant LWP, less water
452 vapor is available per cloud droplet, reducing CER, increasing cloud albedo, and ultimately cooling the
453 atmosphere. This indicates that, in the rapid growth regime, the interaction between AOD and CER in
454 the target region is in agreement with the Twomey effect. The data in Figure 5a show that during period
455 1, S_{CER} varies with buffer size and that the variations are different for different study areas. The value of
456 $|S_{CER}|$ is smallest for the largest study area ($10^\circ \times 10^\circ$) and decreases with buffer size to a minimum for
457 buffer size of 150 km and then increases. For the smallest study area ($4^\circ \times 4^\circ$), the sensitivity exhibits a
458 much stronger negative correlation, with its magnitude decreasing as the buffer size expands, especially
459 for $50 \text{ km} < \text{buffer size} < 100 \text{ km}$. For the 2 intermediate study areas, the sensitivities are initially similar
460 (except for the smallest buffer size) and diverge for $\text{buffer size} > 100 \text{ km}$. The data show that the value of
461 $|S_{CER}|$ overall becomes smaller as study area increases. The decrease of $|S_{CER}|$ with increasing study area
462 is mechanistically tied to scale-dependent aerosol indirect effect theory and meteorological confounding
463 (Quaas et al., 2009; McComiskey & Feingold, 2012). The correlation coefficients R (bottom of Figure 5
464 a) are similar for all four study areas at small buffer sizes, increase fast with buffer size to a maximum
465 for a buffer size of about 50 km and then decrease and diverge. The largest decrease is observed for study
466 area of $10^\circ \times 10^\circ$. In this study, the optimal scale for each study area is indicated in Figure 5 with a red
467 solid square. A plot of the optimal scale versus the size of the study area in Figure 6 (curve LWP1-period1)
468 shows that, as the study area size increased from $6^\circ \times 6^\circ$ to $10^\circ \times 10^\circ$, the optimal scale decreased from
469 100 km to 30 km.

470 As compared with period 1, in period 2 (Figure 5b) the value of the $|S_{CER}|$ also decreases as the buffer
471 size increases. However, the scale sensitivity analysis for period 2 revealed two distinct characteristics
472 different from period 1: (1) the four S_{CER} curves for different study areas are much closer than during
473 period 1; (2) with the exception of the study area of $10^\circ \times 10^\circ$, the values of the $|S_{CER}|$ for the other three
474 study areas are significantly reduced (closer to zero), indicating a corresponding weakening of aerosol-
475 cloud interaction intensity against the background of decreased aerosol concentrations. Particularly

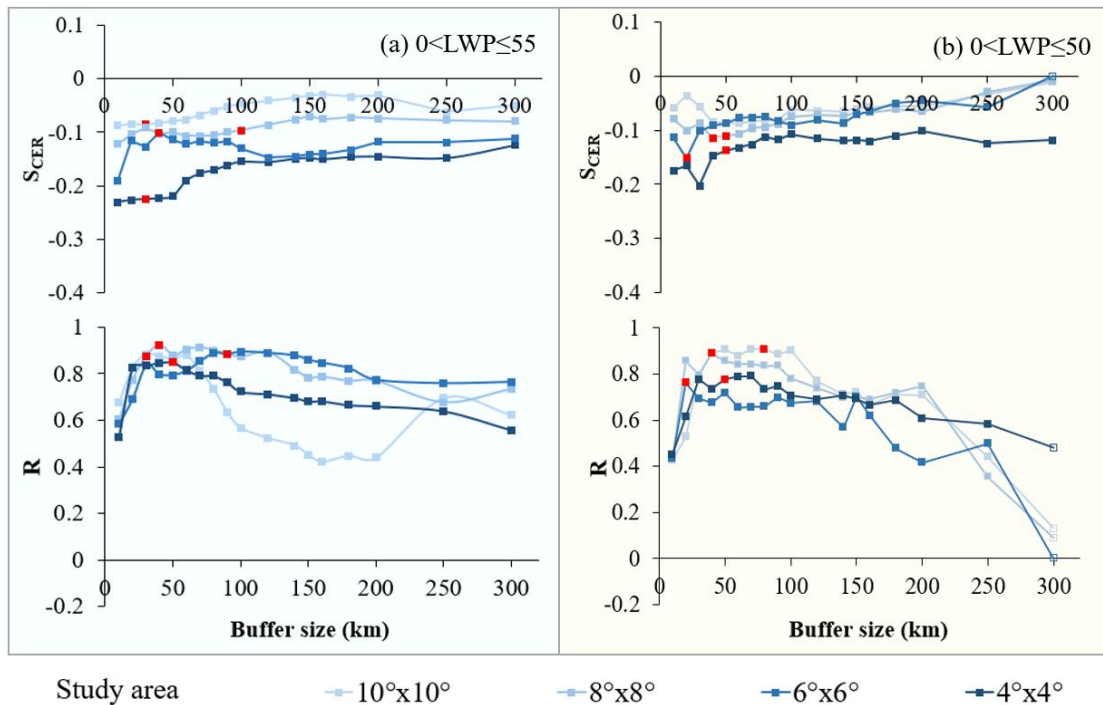
476 noteworthy is that during period 1, the R values for the $10^{\circ}\times 10^{\circ}$ study area showed a sharp declining
477 trend when the buffer size exceeds 60 km, while in period 2 this happened for buffer size larger than 110
478 km and the R value curves for all study areas significantly expanded their high-value ranges. Also for
479 period 2, the R values for the study areas of $10^{\circ}\times 10^{\circ}$ and $8^{\circ}\times 8^{\circ}$ are very similar, in contrast to period 1
480 when only the R values for the study areas of $10^{\circ}\times 10^{\circ}$ decreases fast. Across different study areas, the
481 optimal scale (Curve LWP1-peirod2) shows a behavior opposite to that during period 1: as the study area
482 size increased from $6^{\circ}\times 6^{\circ}$ to $10^{\circ}\times 10^{\circ}$, the optimal scale increased from 20 km to 80 km. It is noted that
483 for a study area of $4^{\circ}\times 4^{\circ}$ the optical scale was 50 km in both periods. For the first LWP regime, S_{CER}
484 estimates and correlation coefficients R by period and optimal buffer size across $4^{\circ}\times 4^{\circ}$ to $10^{\circ}\times 10^{\circ}$ study
485 areas are given in Appendix A1.

486 3.2.2 Decreasing CER regime

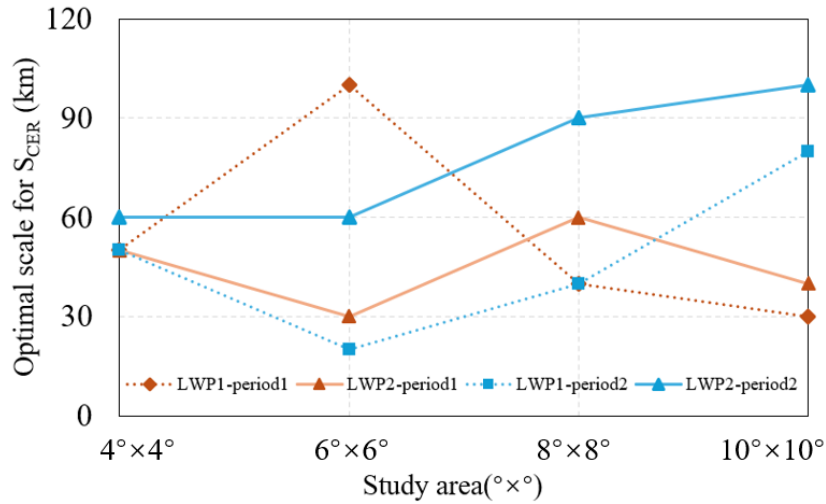
487 During the second LWP regime (Figure 7), the AOD and CER were also negatively correlated ($S_{CER}<0$)
488 during both periods, but the values of S_{CER} vary stronger with the size of study area: the curve dispersion
489 increases in the second LWP regime, the values of $|S_{CER}|$ are larger overall, and the relatively concentrated
490 trend in the period 1 shifts to more scattered fluctuations in the period 2. During period 1, for the largest
491 ($10^{\circ}\times 10^{\circ}$) study area: the value of $|S_{CER}|$ (Figure 7a) decreases with increasing buffer size, nearing zero
492 at ~150 km, briefly turning slightly positive, then slowly falling below zero by 220 km. For the three
493 smaller study areas, the S_{CER} values were all negative and $|S_{CER}|$ overall decreased with increasing buffer
494 size. Through the sensitivity of S_{CER} to buffer size across varying study areas during period 1, the value
495 of $|S_{CER}|$ for a given buffer size becomes smaller with increasing study area size. Additionally, across all
496 study areas, $|S_{CER}|$ initially increases with the increase of the buffer size, then decreases, and gradually
497 stabilizes thereafter. The data in Figure 6 (Curve LWP2-peirod1), show that, the optimal size varies
498 between 30 km and 60 km with no clear dependence on the size of the study area.

499 Compared with period 1, the value of $|S_{CER}|$ in period 2 (Figure 7b) also decreased overall with increasing
500 buffer size, and at the same buffer size, $|S_{CER}|$ decreased as study area increased. However, the scale
501 sensitivity analysis for period 2 revealed two distinct characteristics: (1) the four curves for different
502 study areas are closer than during period 1; (2) the $|S_{CER}|$ for the study area of $10^{\circ}\times 10^{\circ}$ was overall larger,
503 while the values of the S_{CER} curves for the study areas of $4^{\circ}\times 4^{\circ}$ and $6^{\circ}\times 6^{\circ}$ were significantly reduced and

504 that for the study area of $8^\circ \times 8^\circ$ was slightly reduced. The reduction may be attributed to weakened
505 aerosol-cloud interactions resulting from decreased regional aerosol concentrations (Jia et al., 2022; Li
506 et al., 2024; Zhao et al., 2025). The variation of the optimal scale (Curve LWP2-period2) with the size of
507 the study area is similar to that during period 1 in the rapid growth LWP regime: as the study area size
508 increased from $6^\circ \times 6^\circ$ to $10^\circ \times 10^\circ$, the optimal scale increased from 60 km to 100 km. For the second
509 LWP regime, S_{CER} estimates and correlation coefficients R between CER and AOD by period and optimal
510 buffer size across $4^\circ \times 4^\circ$ to $10^\circ \times 10^\circ$ study areas are given in Appendix A1.
511 Through comparative analysis of S_{CER} data distribution across different LWP regimes under different
512 aerosol conditions (i.e. high AOD and decreasing AOD), we found that the $|S_{CER}|$ in the second LWP
513 regime is significantly larger than that in first LWP regime except for the study area of $10^\circ \times 10^\circ$ for buffer
514 size >100 m, where S_{CER} curves corresponding to different study areas show greater dispersion. This
515 pattern highlights the dominant role of LWP in regulating aerosol-cloud interaction sensitivity, with AOD
516 variations further modulating the magnitude of such differences. Sample sizes of CER and AOD for the
517 first LWP regime across both study periods, all buffer sizes and study areas, are presented in Appendices
518 A3–A6.

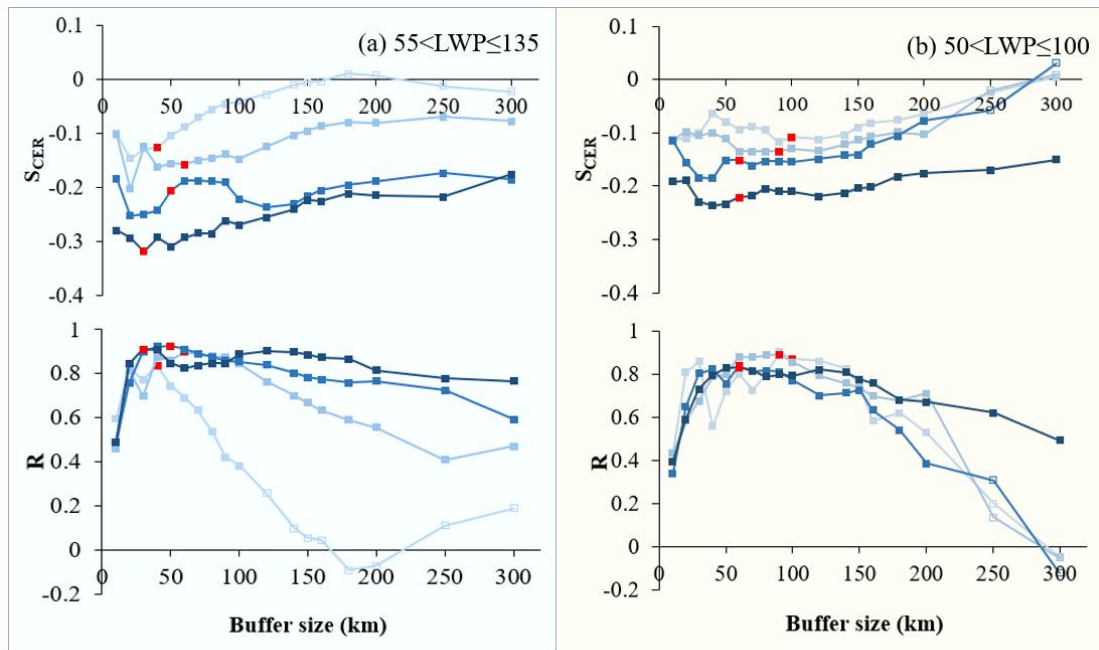


519 Study area $10^\circ \times 10^\circ$ $8^\circ \times 8^\circ$ $6^\circ \times 6^\circ$ $4^\circ \times 4^\circ$
520 Figure 5. Variation of S_{CER} (top) and correlation coefficient R (bottom) with buffer size for different study
521 areas (see legend at the bottom) for (a) the LWP regime with $0 < LWP \leq 55$ g/m² over the years of 2008–2014 and
522 (b) the LWP regime with $0 < LWP \leq 50$ g/m² over the years of 2015–2022. Filled squares indicate that the results
523 are significant at the 0.01 level and open squares indicate that the results are not statistically significant. The
524 red solid squares indicate the optimal buffer sizes for each study area, as shown in the Appendix A1.



525
526
527
528
529
530

Figure 6. Relationship between optimal scale for SCER and the size of the study area. Here LWP1-period1 and LWP2-period1 indicate the optimal scale in period 2008-2014 for the first LWP regime and that for the second LWP regime, respectively. LWP1-period2 and LWP2-period2 indicate the optimal scale in period 2015-2022 for the first LWP regime and that for the second LWP regime, respectively.



Study area —□— 10°x10° —□— 8°x8° —■— 6°x6° —■— 4°x4°

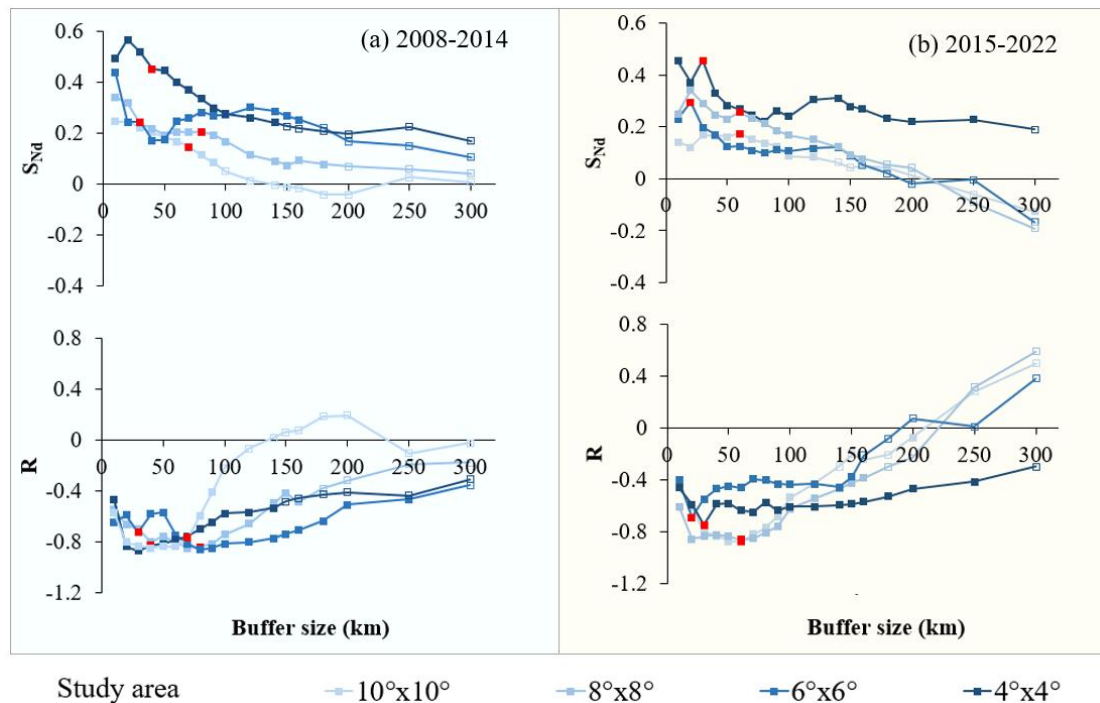
531
532
533
534
535
536
537

Figure 7. Variation of SCER (top) and correlation coefficient R (bottom) with buffer size for different study areas (see legend at the bottom) for (a) the LWP regime with $55 < LWP \leq 135$ g/m² over the years of 2008-2014 and (b) the LWP regime with $50 < LWP \leq 100$ g/m² over the years of 2015-2022. The filled squares indicates that the results are significant at the 0.01 level and the open squares indicates that the results are not statistically significant. The red solid squares indicate the optimal buffer sizes for each study area, as shown in the Appendix A1.

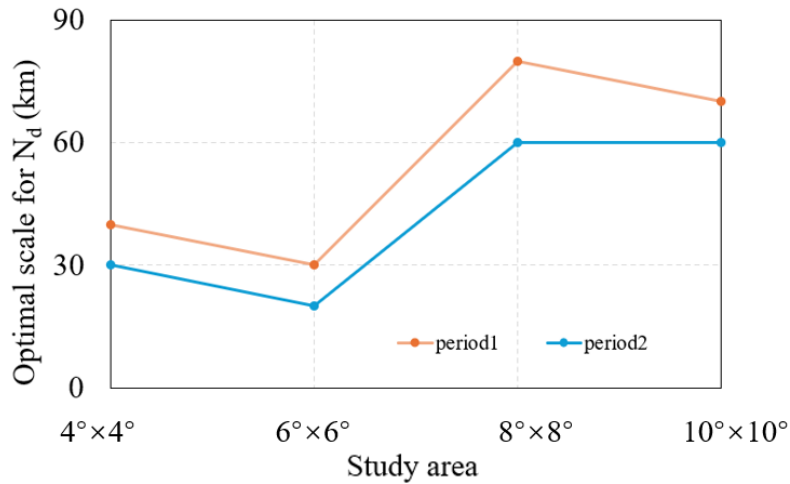
538 3.3 Sensitivity of N_d to AOD

539 Eq. (2) shows that the value of the sensitivity of N_d to AOD is determined by the slope of a linear fit to a
540 log-log plot of N_d versus AOD. To investigate S_{N_d} , we used correlated data pairs for each of the 7 years
541 during periods 1 and 2, binned the data in AOD intervals with a bin width of 0.02, and the N_d data in
542 each AOD bin were averaged. The variation of S_{N_d} with buffer size for different study areas over the
543 target region is presented in Figure 8, for both periods. The data in Figure 8 show that, in contrast to S_{CER} ,
544 S_{N_d} is predominantly positive ($p < 0.01$) during both periods, and decreases with increasing buffer size.
545 During period 1, for the study area of $6^\circ \times 6^\circ$, the S_{N_d} initially decreases very fast to a minimum at a buffer
546 size of 40 to 50 km, followed by an increase to a maximum at a buffer size of 120 km. For buffer size \geq
547 120 km, the S_{N_d} values are similar for the two smallest study areas and substantially larger than for the
548 two larger study areas. During period 2, we can see an initial increase of S_{N_d} for the study area of $6^\circ \times 6^\circ$
549 and $8^\circ \times 8^\circ$, and variation of S_{N_d} for the study area of $10^\circ \times 10^\circ$ and $4^\circ \times 4^\circ$. After that, the S_{N_d} for the study
550 area of $4^\circ \times 4^\circ$ and $6^\circ \times 6^\circ$ decreases very fast to a minimum for a buffer size of 80 km, followed by an
551 increase to a maximum for a buffer size of 140 km. The variation of R with buffer size for each of the
552 two periods shows that the optimal buffer sizes are larger when the study area is larger. Specifically, these
553 optimal sizes in the $8^\circ \times 8^\circ$ and $10^\circ \times 10^\circ$ study areas are larger than those in the $4^\circ \times 4^\circ$ and $6^\circ \times 6^\circ$ areas
554 (Figure 9), reflecting different characteristics in aerosol-cloud interactions in different AOD conditions.
555 The estimates of S_{N_d} and correlation coefficients R between N_d and AOD, stratified by optimal buffer
556 size, for study areas ranging from $4^\circ \times 4^\circ$ to $10^\circ \times 10^\circ$ during the two periods are presented in the Appendix
557 A2. It is noted that S_{CER} and N_d exhibit distinct anomalies in large buffer zones, which may be associated
558 with key factors including aerosol distribution, meteorological heterogeneity, cloud type transitions, and
559 satellite retrieval limitations.
560 The chemical composition of aerosols, which directly affects AOD and CCN activation efficiency,
561 underwent significant changes between the two periods due to policy interventions. During 2008–2014,
562 aerosols over eastern China were dominated by sulfate, which accounted for 30%–40% of the $PM_{2.5}$ mass
563 (Huang et al., 2014; Zheng et al., 2018). Given the strong hygroscopicity of sulfate-dominated aerosols
564 (Zhang et al., 2012; Liu et al., 2023), their CCN activation efficiency was likely high, which may have
565 provided a critical physical basis for the aerosol-cloud indirect effect (Lee et al., 2009). In the period of
566 2015–2022, driven by policies such as the Air Pollution Prevention and Control Action Plan (Zheng et

567 al., 2018), the chemical composition of aerosols underwent a structural transition. Specifically, the mass
 568 fraction of sulfate dropped sharply to 15%–25% with an absolute concentration reduction of more than
 569 50%, while the relative proportions of nitrate, carbonaceous aerosols (i.e., organic carbon (OC) and black
 570 carbon (BC)), and secondary organic aerosols (SOA) showed an increasing trend (Huang et al., 2014;
 571 Zheng et al., 2018). As these components generally exhibit weaker hygroscopicity compared with sulfate
 572 (Zhang et al., 2012; Liu et al., 2023), such a compositional shift might have led to a decrease in CCN
 573 activation efficiency under the same AOD conditions, thereby potentially weakening the sensitivity of
 574 cloud droplet number concentration to AOD and altering the intensity and mode of aerosol-cloud
 575 interactions to a certain extent (Lee et al., 2009).



576 Study area $10^{\circ} \times 10^{\circ}$ $8^{\circ} \times 8^{\circ}$ $6^{\circ} \times 6^{\circ}$ $4^{\circ} \times 4^{\circ}$
 577 **Figure 8.** Variation of S_{Nd} (top) and correlation coefficient R (bottom) with buffer size for different study areas
 578 (see legend **at the bottom**) for the LWP regime with $0 < LWP \leq 200 \text{ g/m}^2$ over the years of 2008-2014 (a) and
 579 2015-2022 (b). The **filled squares** indicates that the results are significant at the 0.01 level and the **open squares**
 580 indicates that the results are not statistically significant. The **red solid square** indicates the optimal buffer size
 581 for each study area, as shown in **the Appendix A2**.



582

583

584

Figure 9. Relationship between optimal scale for N_d and the size of the study area. Here **period1 and **period2** indicate the optimal scale in period 2008-2014 and the optimal scale in period 2015-2022, respectively.**

585

4 Discussion

586

4.1 The importance of **liquid water path constraint**

587

LWP is a critical parameter governing cloud radiative properties (Murray-Watson et al., 2022). The quantification of albedo effects strongly depends on the spatial scale and the LWP. Neglecting LWP constraints in aerosol-cloud interaction studies can weaken microphysical signals, leading to underestimation of radiative forcing (McComiskey et al., 2012). To address this, we first systematically investigated the dynamic relationship between CER and LWP before analyzing CER sensitivity to AOD. The results demonstrate pronounced CER sensitivity to LWP variations, which can be categorized into three distinct **regimes (Figure 4)**:

594

In the first LWP regime, CER increases rapidly with LWP, **i.e. the evolution of CER is predominantly driven by changes in LWP**. This dominance may lead to overestimation of the influence of the AOD on CER (Liu et al., 2021).

597

In the second LWP regime, CER decreases with increasing LWP. **In** this regime, the regulatory effect of LWP on CER weakens significantly, and CER variations become increasingly governed by aerosol-related processes, indicating the growing dominance of aerosol indirect effects.

600

The third regime contains an insufficient number of CER observations to yield statistically significant results, **which excludes the** analysis of the sensitivity of CER to AOD.

602

Comparative analysis of scale-conditioned S_{CER} across LWP regimes in periods 1 and 2 revealed

603 markedly enhanced sensitivity of S_{CER} to AOD in the second LWP regime. There is a trade-off between
604 AOD and LWP when the amount of water vapor is insufficient and CER becomes smaller. As suggested
605 by Costantino et al. (2013), the LWP response to aerosol invigoration is influenced by two competing
606 mechanisms: a drying effect caused by enhanced entrainment of dry air at cloud top (dominant in
607 optically thin clouds) and a moistening effect from precipitation suppression (dominant in optically thick
608 clouds). For larger LWP, the supply of cloud water is sufficient, and the increase in aerosol number
609 concentrations significantly affects the distribution of cloud droplet number concentrations and sizes,
610 enhancing the sensitivity of CER to AOD. For small aerosol concentrations, the values of $|S_{CER}|$ (Figure
611 5b, 7b) decreased overall with expanding buffer size within the same study area. For fixed buffer size,
612 $|S_{CER}|$ decreased as the study area increased, and the ranges of $|S_{CER}|$ values across different study area
613 showed a convergent pattern, typically remaining small (close to zero). During the high AOD period
614 (2008–2014), anthropogenic emissions and dust transport provided abundant CCN, laying the material
615 foundation for aerosol-cloud interactions. This enhanced the synergistic effect of “sufficient liquid water
616 + abundant CCN” in the second LWP regime, amplifying the difference in S_{CER} between the two LWP
617 regimes. In the period of decreasing AOD (2015–2022), following the implementation of clean air
618 policies (de Leeuw et al., 2021; 2023), CCN concentration decreased (Wang et al, 2023), weakening the
619 direct impact of aerosols on CER. However, the LWP-driven microphysical differences persisted, so S_{CER}
620 in the second regime remained significantly smaller than that in the first regime, albeit with a smaller
621 difference. Additionally, the complexity of aerosol types during the high AOD period (e.g., mixing of
622 anthropogenic pollutants and natural dust) may have adjusted the value of S_{CER} , but did not alter the
623 dominant role of LWP. This aligns with the theory that “aerosol indirect effects are jointly regulated by
624 concentration and type” (Liu et al., 2017).

625 The larger S_{CER} observed at larger spatial scales (Figures 5 and 7) may be attributed to meteorological
626 confounding effects. In addition, clouds with larger LWP are usually associated with strong updrafts
627 (such as convective clouds), and stronger turbulence and vertical transport will bring more aerosols into
628 the clouds, increasing CCN concentration and a decrease in particle size, making them more sensitive to
629 changes in AOD (Jones et al., 2009; Han et al., 2022; Fan et al., 2025). Therefore, this phenomenon is
630 the result of the combined action of cloud microphysical processes (CCN activation, cloud droplet
631 competition growth) and dynamic processes (updrafts, turbulent mixing). If the characteristics of aerosols

632 (such as composition) change in the second LWP regime, this sensitivity may be further amplified.
633 Consequently, the LWP-stratified S_{CER} quantification framework enables precise characterization of
634 scale-dependent aerosol-cloud interactions, providing robust physical insights for climate effect
635 assessments and effectively reducing uncertainties in future climate projections.

636 The central hypothesis of this study—that LWP is relatively consistent between the two periods (2008–
637 2014 and 2015–2022), supporting valid comparisons of the spatial sensitivity of AOD-CER
638 relationships—is well-supported by the following analysis. The differences in the mean, median, 25th,
639 and 50th percentiles of LWP between the two periods are all less than 5%, indicating a stable overall
640 water vapor supply level. The spatial patterns of high-LWP regions (e.g., southeastern areas) and low-
641 LWP regions (e.g., the mountainous areas in northern Shanxi) remained stable across the two periods
642 (see Appendix B1), demonstrating LWP spatial distribution characteristics are highly consistent. The
643 sample proportions of LWP in the rapid growth regime are 59.30% (period 1: 0–55 g/m²) and 55.36%
644 (period 2: 0–50 g/m²), while those in the decreasing regime are 29.64% (period 1: 55–135 g/m²) and
645 24.59% (period 2: 50–100 g/m²), suggesting that there is no systematic temporal shift in the LWP
646 distribution. Meanwhile, short-term fluctuations are smoothed by multi-year averaging and large-sample
647 statistics, resulting in a weak indirect impact of aerosols on LWP (LWP only increased by 5.6%, much
648 smaller than the 24% decrease in AOD). Additionally, LWP-stratified analysis further isolates
649 interference. The validation of the core hypothesis provides a reliable premise for accurately quantifying
650 the impact of aerosol concentration changes on the sensitivity of cloud parameters and their spatial scale
651 dependence.

652 4.2 Scale dependence of cloud parameters sensitivities to aerosol variations

653 Extensive studies have demonstrated a significant spatial scale dependence of aerosol indirect effects
654 (McComiskey et al., 2012; Possner et al., 2016; Glotfelty et al., 2020; Ekman et al., 2023). Failure to
655 explicitly define the scale-dependent behavior of aerosol indirect effects may introduce systematic biases
656 and inconsistencies in subsequent process analyses. Based on satellite observations, this study confirms
657 statistically significant negative correlations between CER and AOD, as well as positive correlations
658 between N_d and AOD during periods with different aerosol concentrations, aligning with classical
659 aerosol-cloud interaction theory (Quaas et al., 2009). Analysis of scale-conditioned S_{CER} and S_{N_d} reveals

660 that for fixed buffer size, an increase in the size of the study area leads to a systematic reduction in S_{CER}
661 (less negative) and S_{Nd} , corroborating the nonlinear attenuation of aerosol signals with spatial domain
662 expansion (Quaas et al., 2009). The results from this study suggest that AOD-cloud property correlations
663 in large study areas are susceptible to meteorological confounding effects (Quaas et al., 2010; Boucher
664 and Quaas, 2012; Gryspeerdt et al., 2014; Liu et al., 2024). Theoretically, aerosol regulation of cloud
665 microphysics is strongly local: smaller domains (e.g., $4^\circ \times 4^\circ$) feature homogeneous meteorological
666 conditions (humidity, updrafts), preserving undiluted aerosol-cloud interaction signals and yielding larger
667 $|S_{CER}|$ (pronounced Twomey effect). In contrast, expanded domains (e.g., $10^\circ \times 10^\circ$) encompass
668 heterogeneous meteorological conditions (circulation differences, boundary layer variability) that
669 independently modulate cloud droplet growth. For example, strong updrafts enhance liquid water supply,
670 offsetting aerosol-induced radius reduction (Altartatz et al., 2014), weakening aerosol-CER correlations
671 and reducing $|S_{CER}|$. Consistent with Grandey & Stier (2010), large-scale domains introduce “dilution
672 bias” via non-target meteorological variability. This scale-dependent confounding mechanism elucidates
673 uncertainties in aerosol indirect effect assessments at regional scales.

674 Multi-scale spatial analysis identifies different optimal buffer sizes for S_{CER} and S_{Nd} in different periods.
675 These findings align closely with satellite-based aerosol indirect effect studies (Wang et al., 2015; Liu et
676 al., 2017), providing critical scale benchmarks for satellite product validation. Wang et al. (2015) reported
677 an inverse “Twomey” effect between aerosols and CER in eastern China by analyzing aerosol and CER
678 within a 50 km buffer zone around CALIOP samples. Similarly, Liu et al. (2017) systematically examined
679 the response mechanisms of warm cloud macro- and microphysical parameters to increasing AOD in the
680 Yangtze River Delta region, also using CALIOP samples within a 50 km buffer zone. Present study
681 further shows that, as aerosol concentrations decrease, S_{CER} values across different study areas with the
682 same buffer size exhibit convergence characteristics, with generally smaller S_{CER} (closer to zero). This
683 indicates a significant weakening of aerosol-cloud interaction intensity and reduced spatial extent
684 dependency in low aerosol loading conditions. This phenomenon is consistent with the simulated
685 behavior of aerosol-limited cloud regimes, where aerosol-cloud interactions are quantitatively modulated
686 by moisture availability and lose their sensitivity to large-scale dynamical stability, leading to a weaker
687 and more homogeneous effect (Zhao et al., 2025).

688 By systematically quantifying the scale-response characteristics of aerosol indirect effects, this work not

689 only elucidates the dynamic scale behavior of aerosol-cloud interactions but, more critically, establishes
690 criteria for determining optimal buffer size in regional aerosol indirect effect studies. Such advancements
691 provide actionable insights for refining parameterization schemes in climate models, thereby enhancing
692 their predictive reliability.

693 **4.3 Contrasting sensitivity patterns of cloud parameters in response to AOD**

694 A comprehensive comparison of the sensitivity S_{CER} and S_{Nd} reveals that the responses of CER and N_d to
695 AOD exhibit distinct yet inherently interconnected characteristics. These characteristics are jointly
696 modulated by spatial scale and LWP regimes (Figs. 5, 7, 8; Appendices A1–A2), which profoundly reflect
697 the core microphysical mechanisms of aerosol-cloud interactions. Details are elaborated as follows:

698 **4.3.1 Core differences in response modes between S_{CER} and N_d to AOD**

699 S_{CER} is consistently negative across both periods and all LWP regimes ($-0.33 < S_{CER} < 0$) (Figs. 5, 7;
700 Appendix A1), indicating that an increase in AOD leads to a decrease in CER. This aligns with the core
701 principle of the Twomey effect (Twomey, 1977; Feingold et al., 2001). The values of $|S_{CER}|$ are larger in
702 the second LWP regime than in the first regime, reflecting stronger aerosol modulation of cloud
703 microphysical properties when liquid water is abundant (McComiskey & Feingold, 2012). In contrast,
704 S_{Nd} maintains a significant positive correlation with AOD across all scenarios ($0 < S_{Nd} < 1$) (Fig. 8;
705 Appendix A2), confirming that higher AOD directly promotes CCN activation and thereby increases
706 cloud droplet number concentration (Andreae, 2009). S_{Nd} is larger in small-scale study areas (e.g., $4^\circ \times 4^\circ$)
707 and small buffer zones, with a maximum value of 0.45 in the first period, indicating greater sensitivity
708 of cloud droplet number to aerosol loading at fine spatial scales.

709 **4.3.2 Synergistic modulation of AOD and spatial scale**

710 Using the LWP interval corresponding to S_{Nd} ($0 < LWP \leq 200 \text{ g/m}^2$) as a benchmark, comparisons
711 between the two periods (incorporating average values of S_{CER} across two LWP regimes) reveal distinct
712 characteristics:

713 For the small-scale study area ($4^\circ \times 4^\circ$): In period 1, the average $|S_{CER}|$ across two LWP regimes is 0.271
714 (0.2232 for the $0\text{--}55 \text{ g/m}^2$ LWP regime, 0.3189 for the $55\text{--}135 \text{ g/m}^2$ LWP regime) and $S_{Nd}=0.4496$, both

715 significantly higher than those in period 2 (average $|S_{CER}|=0.154$, with 0.0863 for 0–50 g/m² LWP regime
716 and 0.2212 for 50–100 g/m² LWP regime; $S_{Nd}=0.2903$). The negative correlation between AOD and CER
717 is more significant in period 1, as sufficient CCN in small-scale areas amplifies both cloud droplet
718 number increase and size reduction, enhancing the Twomey effect.
719 For the medium-to-large scale study areas (6°×6°, 8°×8°, 10°×10°): In period 1, the average $|S_{CER}|$ across
720 two LWP regimes is 0.1683 (0.1305 for 0–55 g/m², 0.2061 for 55–135 g/m²), 0.13065 (0.1026 for 0–55
721 g/m², 0.1587 for 55–135 g/m²), and 0.1067 (0.0858 for 0–55 g/m², 0.0885 for 55–135 g/m²), respectively,
722 all higher than the corresponding values in period 2 (0.1516, 0.1246, 0.0985). However, S_{Nd} in period 1
723 (0.2430, 0.2050, 0.1430) is lower than that in period 2 (0.2960, 0.2680, 0.1740), with no significant
724 difference in the negative correlation between AOD and CER between the two periods.
725 This characteristic indicates that meteorological confounding effects are enhanced at larger scales,
726 weakening the regulation of S_{Nd} by aerosols, while at small scales the aci is directly driven by AOD levels.

727 **4.3.3 Implications for aerosol indirect effects**

728 The differences and interconnections between S_{CER} and S_{Nd} highlight that aerosol indirect effects are
729 dominated by coupled microphysical processes: Aerosol-induced increases in CCN first enhance N_d
730 through positive S_{Nd} , and then reduce CER through negative S_{CER} under constant LWP conditions. The
731 scale-dependent attenuation of both sensitivities and their modulation by LWP indicate that quantifying
732 aerosol indirect effects requires full consideration of spatial scales and the key role of liquid water,
733 providing observational basis for optimizing climate model parameterization schemes.

734 **4.4 Limitations and future perspectives**

735 This study has three significant limitations. Firstly, similar to most previous studies (Wang et al., 2015;
736 Liu et al., 2021), this study only utilized MODIS data with a resolution of 10 km to explore scale effects,
737 ignoring finer or coarser resolution data. Therefore, using a 10 km buffer size as the minimum
738 observation unit, this limitation makes the indirect effects of aerosols on smaller scales still unknown,
739 which may lead to inaccurate evaluation of aerosol indirect effects. Therefore, future research can
740 improve the sensitivity of aerosol indirect effects to scale changes by using observation data with higher
741 accuracy or model simulations. Secondly, the current research focuses on the influence of buffer size and

742 study areas, the potential impact of spatial aggregation methods (especially zoning directionality) on the
743 quantitative results of aerosol indirect effects has not been systematically evaluated. Future research
744 should further investigate the sensitivity of aerosol indirect effects to zoning direction. Moreover, the
745 current study employs a uniform buffer size for both aerosol and cloud parameters, failing to account for
746 potential interaction effects arising from discrepancies of buffer size between them. Therefore, clarifying
747 scale dependence will avoid directly extrapolating local observation results to a larger study area when
748 downscaling climate models or formulating regional environmental policies.

749 **5 Conclusions**

750 Based on MODIS and CALIOP satellite observations of aerosol and cloud parameters over land in eastern
751 China, a comparative analysis **was conducted** of the sensitivity of cloud microphysical parameters (CER
752 and N_d) to variations in AOD during two characteristic periods: **2008–2014 (period 1, high AOD) and**
753 **2015–2022 (period 2, decreasing AOD)**. Through systematic analysis of the relationship between CER
754 and LWP and their response mechanisms to AOD across these two periods, the following key conclusions
755 were drawn:

756 Firstly, CER exhibited three distinct **regimes** with varying LWP. During the rapid growth regime (LWP
757 $< 55/50$ g/m²), CER showed significant negative sensitivity to AOD (S_{CER}), consistent with the Twomey
758 effect; during the **decreasing** regime (LWP = 55-135/50-100 g/m²), S_{CER} remained negative but with
759 enhanced sensitivity; and during the slow growth regime (LWP $> 135/100$ g/m²), the rate of CER change
760 significantly decreased. These findings confirmed that LWP is a crucial, regulatory factor influencing the
761 CER response to AOD.

762 Secondly, scale dependence analysis **led to the conclusion that characteristics in aerosol-cloud interaction**
763 **are significantly scale-dependent, with systematic variations of both S_{CER} and S_{Nd} with changes in buffer**
764 **size and study area**. The results of the study show that S_{CER} systematically **increased as buffer size**
765 **increased and became** negligible for buffer sizes larger than 150-200 km, while the optimal buffer sizes
766 varied substantially with the size of the study area in the range from $6^\circ \times 6^\circ$ to $10^\circ \times 10^\circ$: **increased as study**
767 **area increased during period 2, but decreased** in period 1 for regime 2. Particularly noteworthy **is the**
768 **enhanced consistency of S_{CER} across different study areas and the significant increase in S_{CER} during**
769 period 2, reflecting weaker aerosol-cloud interactions due to declining regional aerosol concentrations.

770 Finally, the sensitivity of N_d to AOD (S_{N_d}) exhibited distinct characteristics compared to S_{CER} : S_{N_d} showed
771 a significant positive correlation ($p < 0.01$) and demonstrated nonlinear attenuation with increasing buffer
772 size and study area. The optimal buffer size for S_{N_d} was smaller during period 2 than during period 1 and
773 increased with the study area size, being substantially larger for study areas of $8^\circ \times 8^\circ$ and $10^\circ \times 10^\circ$ than
774 for study areas of $4^\circ \times 4^\circ$ and $6^\circ \times 6^\circ$ areas. These findings not only deepen our understanding of aerosol
775 indirect effects but also provide an important observational basis for improving aerosol-cloud
776 parameterization schemes in climate models. The results emphasize that both the phased characteristics
777 of LWP and spatial scale effects must be considered when assessing aerosol indirect effects.

778 Appendix

779 **A1. Estimates of S_{CER} , computed using Eq. (1), and correlation coefficients R between CER and AOD,**
780 **stratified by LWP, and optimal buffer size (see text), for study areas varying from $4^\circ \times 4^\circ$ to $10^\circ \times 10^\circ$, during**
781 **the periods 2008-2014 and 2015-2022. Statistically significant data points are indicated with * (p value < 0.01).**

Years	LWP (g/m^2)	Study area	Optimal scale (km)	S_{CER}	R
2008-2014	0-55	$10^\circ \times 10^\circ$	30	-0.0858	0.8828*
		$8^\circ \times 8^\circ$	40	-0.1026	0.9220*
		$6^\circ \times 6^\circ$	100	-0.1305	0.8939*
		$4^\circ \times 4^\circ$	50	-0.2232	0.8459*
	55-135	$10^\circ \times 10^\circ$	40	-0.1275	0.8377*
		$8^\circ \times 8^\circ$	60	-0.1587	0.8978*
		$6^\circ \times 6^\circ$	30	-0.2061	0.9245*
		$4^\circ \times 4^\circ$	50	-0.3189	0.9096*
2015-2022	0-50	$10^\circ \times 10^\circ$	80	-0.0885	0.9082*
		$8^\circ \times 8^\circ$	40	-0.1138	0.8886*
		$6^\circ \times 6^\circ$	20	-0.1517	0.7618*
		$4^\circ \times 4^\circ$	50	-0.0863	0.6403*
	50-100	$10^\circ \times 10^\circ$	100	-0.1084	0.8717*
		$8^\circ \times 8^\circ$	90	-0.1354	0.8910*
		$6^\circ \times 6^\circ$	60	-0.1514	0.8384*
		$4^\circ \times 4^\circ$	60	-0.2212	0.8318*

782
783
784
785
786
787
788
789
790

791 A2. Estimates of S_{Na} , computed using Eq. (2), and correlation coefficients R between N_d and AOD, stratified
 792 by optimal buffer size (see text) for study areas varying from $4^\circ \times 4^\circ$ to $10^\circ \times 10^\circ$, during the periods 2008-2014
 793 and 2015-2022. Statistically significant data points are indicated with * (p value < 0.01).

Years	Study area	Optimal scale (km)	S_{Na}	R
2008-2014	$10^\circ \times 10^\circ$	70	0.1434	-0.8507*
	$8^\circ \times 8^\circ$	80	0.2045	-0.8646*
	$6^\circ \times 6^\circ$	30	0.2430	-0.8741*
	$4^\circ \times 4^\circ$	40	0.4496	-0.8523*
2015-2022	$10^\circ \times 10^\circ$	60	0.1742	-0.8788*
	$8^\circ \times 8^\circ$	60	0.2682	-0.8638*
	$6^\circ \times 6^\circ$	20	0.2964	-0.6900*
	$4^\circ \times 4^\circ$	30	0.2903	-0.7478*

794

795 A3. Sample sizes of cloud droplet effective radius (CER) and aerosol optical depth (AOD) across different
 796 buffer sizes, study areas (LWP regime 1, 2008–2014).

Buffer sizes	Sample sizes of CER in LWP regime 1				Sample sizes of AOD in LWP regime 1			
	$10^\circ \times 10^\circ$	$8^\circ \times 8^\circ$	$6^\circ \times 6^\circ$	$4^\circ \times 4^\circ$	$10^\circ \times 10^\circ$	$8^\circ \times 8^\circ$	$6^\circ \times 6^\circ$	$4^\circ \times 4^\circ$
10	25054	16133	8551	3879	47846	32406	18711	8808
20	41667	26507	14077	6376	64878	42949	24462	11377
30	54960	34885	18421	8346	76569	50055	28274	13047
40	66170	42147	22136	9966	86291	56006	31523	14482
50	76207	48769	25738	11593	94726	61227	34272	15664
60	85194	54539	28946	12979	102262	65860	36741	16695
70	93413	59681	31788	14192	108792	69756	38749	17519
80	100728	64370	34330	15317	114357	73103	40498	18246
90	107291	68535	36552	16270	119187	76077	42016	18893
100	113457	72525	38761	17155	123607	78839	43496	19469
120	124793	79882	42945	18964	131449	83807	46217	20534
140	134597	86324	46525	20462	138140	88001	48518	21557
150	138760	89086	48145	21141	141012	89985	49570	21991
160	142693	91808	49602	21734	143725	91767	50570	22436
180	150015	96789	52326	22860	148480	94870	52385	23155
200	156655	101246	54894	23983	153084	97946	53963	23921
250	169423	109475	59449	26008	162530	104346	56987	25388
300	178015	115051	62656	27442	170117	109006	59332	26453

797

798 A4. Sample sizes of cloud droplet effective radius (CER) and aerosol optical depth (AOD) across different
 799 buffer sizes, study areas (LWP regime 2, 2008–2014).

Buffer sizes	Sample sizes of CER in LWP regime 2				Sample sizes of AOD in LWP regime 2			
	$10^\circ \times 10^\circ$	$8^\circ \times 8^\circ$	$6^\circ \times 6^\circ$	$4^\circ \times 4^\circ$	$10^\circ \times 10^\circ$	$8^\circ \times 8^\circ$	$6^\circ \times 6^\circ$	$4^\circ \times 4^\circ$
10	22338	14357	7737	3715	47846	32406	18711	8808
20	35406	22471	11964	5697	64878	42949	24462	11377
30	45473	28805	15162	7187	76569	50055	28274	13047
40	54074	34078	17839	8368	86291	56006	31523	14482

50	61579	38732	20290	9444	94726	61227	34272	15664
60	68173	43017	22553	10424	102262	65860	36741	16695
70	74272	46909	24584	11230	108792	69756	38749	17519
80	79999	50507	26412	11950	114357	73103	40498	18246
90	85339	53806	28177	12654	119187	76077	42016	18893
100	90440	56944	29812	13329	123607	78839	43496	19469
120	99758	62598	32673	14486	131449	83807	46217	20534
140	108723	68273	35600	15795	138140	88001	48518	21557
150	112740	70969	36864	16426	141012	89985	49570	21991
160	116558	73463	38046	16974	143725	91767	50570	22436
180	123653	78031	40203	17917	148480	94870	52385	23155
200	129864	81813	42186	18674	153084	97946	53963	23921
250	142429	89112	46079	20120	162530	104346	56987	25388
300	152460	95213	49452	21369	170117	109006	59332	26453

800

801

802

A5. Sample sizes of cloud droplet effective radius (CER) and aerosol optical depth (AOD) across different buffer sizes, study areas (LWP regime 1, 2015–2022).

Buffer sizes	Sample sizes of CER in LWP regime 1				Sample sizes of AOD in LWP regime 1			
	10°×10°	8°×8°	6°×6°	4°×4°	10°×10°	8°×8°	6°×6°	4°×4°
10	25054	16133	8551	3879	47846	32406	18711	8808
20	41667	26507	14077	6376	64878	42949	24462	11377
30	54960	34885	18421	8346	76569	50055	28274	13047
40	66170	42147	22136	9966	86291	56006	31523	14482
50	76207	48769	25738	11593	94726	61227	34272	15664
60	85194	54539	28946	12979	102262	65860	36741	16695
70	93413	59681	31788	14192	108792	69756	38749	17519
80	100728	64370	34330	15317	114357	73103	40498	18246
90	107291	68535	36552	16270	119187	76077	42016	18893
100	113457	72525	38761	17155	123607	78839	43496	19469
120	124793	79882	42945	18964	131449	83807	46217	20534
140	134597	86324	46525	20462	138140	88001	48518	21557
150	138760	89086	48145	21141	141012	89985	49570	21991
160	142693	91808	49602	21734	143725	91767	50570	22436
180	150015	96789	52326	22860	148480	94870	52385	23155
200	156655	101246	54894	23983	153084	97946	53963	23921
250	169423	109475	59449	26008	162530	104346	56987	25388

803

804

805

A6. Sample sizes of cloud droplet effective radius (CER) and aerosol optical depth (AOD) across different buffer size, study areas (LWP regime 2, 2015–2022).

Buffer sizes	Sample sizes of CER in LWP regime 2				Sample sizes of AOD in LWP regime 2			
	10°×10°	8°×8°	6°×6°	4°×4°	10°×10°	8°×8°	6°×6°	4°×4°
10	6548	6548	5449	2803	12892	12892	12892	5961
20	24886	16258	8833	4421	46067	30536	17623	8079

30	32260	20786	11214	5490	55767	36685	20780	9408
40	38784	24739	13284	6440	63457	41493	23310	10474
50	44831	28399	15176	7183	70030	45443	25423	11419
60	50181	31609	16909	7816	75667	48900	27138	12122
70	54865	34476	18456	8415	80872	51807	28559	12723
80	58946	37042	19776	8901	85308	54361	29846	13245
90	62835	39437	21006	9359	89202	56659	31024	13706
100	66623	41757	22165	9796	92939	58931	32143	14126
120	73427	46010	24248	10605	99298	62674	34081	14927
140	79486	49854	26210	11312	104540	65994	36013	15617
150	82336	51650	26988	11633	107089	67545	36876	15939
160	85055	53440	27893	11942	109626	69104	37718	16261
180	89669	56388	29401	12520	114187	72088	39380	16889
200	93898	58986	30700	13034	117969	74508	40596	17401
250	102933	64417	33649	14040	125590	79489	43005	18271
300	109964	68913	35755	14701	132000	83404	45012	18913

806

807 **A7. Sample sizes of cloud droplet number concentration (N_d) and aerosol optical depth (AOD) across different**
808 **buffer sizes and study areas during 2008-2014.**

Buffer sizes	Sample sizes of N _d				Sample sizes of AOD			
	10°×10°	8°×8°	6°×6°	4°×4°	10°×10°	8°×8°	6°×6°	4°×4°
10	47846	32406	18711	8808	50686	32611	17320	8053
20	64878	42949	24462	11377	70102	45066	23944	11084
30	76569	50055	28274	13047	84442	54334	28822	13435
40	86291	56006	31523	14482	96186	62056	32857	15309
50	94726	61227	34272	15664	106166	68620	36473	16906
60	102262	65860	36741	16695	114950	74328	39638	18292
70	108792	69756	38749	17519	122840	79508	42510	19478
80	114357	73103	40498	18246	129763	84048	45038	20599
90	119187	76077	42016	18893	135810	87931	47225	21548
100	123607	78839	43496	19469	141407	91543	49256	22436
120	131449	83807	46217	20534	151353	98040	53031	24145
140	138140	88001	48518	21557	159758	103516	56167	25517
150	141012	89985	49570	21991	163180	105820	57561	26100
160	143725	91767	50570	22436	166373	108000	58769	26661
180	148480	94870	52385	23155	172007	111773	60981	27665
200	153084	97946	53963	23921	176658	114922	62862	28696
250	162530	104346	56987	25388	185393	120627	66331	30409
300	170117	109006	59332	26453	191138	124592	68823	31481

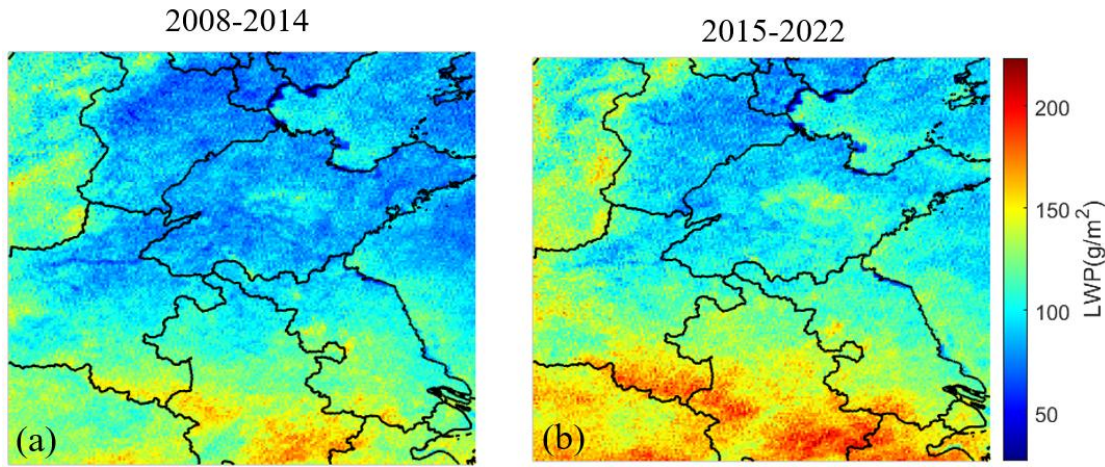
809

810 **A8. Sample sizes of cloud droplet number concentration (N_d) and aerosol optical depth (AOD) across different**
811 **buffer sizes and study areas during 2015-2022.**

Buffer sizes	Sample sizes of N _d				Sample sizes of AOD			
--------------	--------------------------------	--	--	--	---------------------	--	--	--

	10°×10°	8°×8°	6°×6°	4°×4°	10°×10°	8°×8°	6°×6°	4°×4°
10	37182	23994	13048	6149	31621	21503	12892	5961
20	51313	32990	17755	8252	46067	30536	17623	8079
30	61921	39800	21327	9788	55767	36685	20780	9408
40	70663	45351	24213	11063	63457	41493	23310	10474
50	78059	50080	26808	12118	70030	45443	25423	11419
60	84354	53975	28967	13015	75667	48900	27138	12122
70	89675	57448	30881	13832	80872	51807	28559	12723
80	94620	60671	32636	14556	85308	54361	29846	13245
90	99042	63497	34138	15155	89202	56659	31024	13706
100	102936	65993	35444	15703	92939	58931	32143	14126
120	110590	70884	38002	16787	99298	62674	34081	14927
140	116487	74472	40007	17549	104540	65994	36013	15617
150	119140	76230	41049	17958	107089	67545	36876	15939
160	121506	77846	41958	18265	109626	69104	37718	16261
180	125788	80845	43582	18935	114187	72088	39380	16889
200	129613	83370	44887	19538	117969	74508	40596	17401
250	136752	87967	47756	20784	125590	79489	43005	18271
300	141896	91273	49807	21431	132000	83404	45012	18913

812



813

814 **B1. Spatial distributions of LWP averaged over the years 2008-2014 (a) and 2015-2022 (b) over the study area.**

815 **The lines are provincial borders and the names of provinces mentioned in the text are indicated in Fig. 3(f).**

816 **Data availability**

817 All data used in this study are publicly available. The satellite data from the MODIS instrument used in

818 this study were obtained from <https://ladsweb.nascom.nasa.gov/search/> (last access: 02 July 2025). The

819 satellite data from CALIOP were obtained from <https://subset.larc.nasa.gov/calipso/login.php> (last

820 access: 02 July 2025).

821 **Author contributions**

822 YL, LT and GL designed the research. YL and LT led the analyses. YL and GL wrote the manuscript
823 with major input from JH, and further input from all other authors. All authors contributed to interpreting
824 the results and to the finalization and revision of the manuscript.

825 **Competing interests**

826 The authors declare that they have no conflict of interest.

827 **Acknowledgements**

828 The authors greatly appreciate NASA CloudSat Data Processing Center that provided the data used in
829 this study. This work was supported by the National Natural Science Foundation of China (Grant No.
830 42001290), the National Natural Science Foundation of China (Grant No. 42271299), the Natural Science
831 Foundation Project of Xiamen (Grant No. 3502Z202472037) and the Chinese Academy of Sciences
832 President's International Fellowship Initiative, Grant No. 2025PVA0014_Y1.

833 **References**

- 834 Albrecht, B. A.: Aerosols, cloud microphysics, and fractional cloudiness, *Science*, 245, 1227-1230, 1989.
- 835 Bellouin, N., Quaas, J., Gryspeerdt, E., Kinne, S., Stier, P., Watson-Parris, D., et al.: Bounding global
836 aerosol radiative forcing of climate change. *Reviews of Geophysics*, 58, e2019RG000660.
837 <https://doi.org/10.1029/2019RG000660>, 2020.
- 838 Altaratz, O., Koren, I., Remer, L.A., Hirsch, E.: Review: Cloud invigoration by aerosols—Coupling
839 between microphysics and dynamics. *Atmospheric Research*, 140-141, 38-60, 2014.
- 840 Andreae, M. O.: Correlation between cloud condensation nuclei concentration and aerosol optical
841 thickness in remote and polluted regions, *Atmos. Chem. Phys.*, 9, 543-556, [https://doi.org/10.5194/acp-](https://doi.org/10.5194/acp-9-543-2009)
842 [9-543-2009](https://doi.org/10.5194/acp-9-543-2009), 2009.
- 843 Baum, B. A., et al.: MODIS cloud-top property refinement for Collection 6, *J. Appl. Meteorol. Climatol.*,
844 [51\(6\), 1145-1163](https://doi.org/10.1175/JAP1163), 2012.

845 Bender, F.A.M., Frey, L., McCoy, D.T., Grosvenor, D.P., Mohrmann, J.K.: Assessment of aerosol–
846 cloud–radiation correlations in satellite observations, climate models and reanalysis. *Climate Dynamics*,
847 52, 4371-4392, 2019.

848 Boucher, O., Quaas, J.: Water vapour affects both rain and aerosol optical depth. *Nature Geoscience*, 6(1),
849 4-5. <https://doi.org/10.1038/ngeo1692>, 2012.

850 Bréon, F. M., Tanré, D., Generoso, S.: Aerosol effect on cloud droplet size monitored from satellite,
851 *Science*, 295(5556):834-8. doi: 10.1126/science.1066434, 2002.

852 Bulgin, C. E., Palmer, P.I., Thomas, G.E., Arnold, C.P.G., Campmany, E., Carboni, E., Grainger, R. G.,
853 Poulsen, C., Siddans, R., Lawrence, B.N.: Regional and seasonal variations of the Twomey indirect effect
854 as observed by the ATSR-2 satellite instrument, *Geophysical Research Letters*, 35, 2, 2008.

855 Cai, H., Yang, Y., Chen, Q.: Distribution Characteristics of Cloud Types and Cloud Phases over China
856 and Their Relationship with Cloud Temperature, *Remote Sensing*, 14(21), 2022.
857 <https://doi.org/10.3390/rs14215601>

858 Chen, G., W.-C.Wang, and J.-P. Chen, 2015: Aerosol–stratocumulus–radiation interactions over
859 southeast Pacific. *J. Atmos. Sci.*, 72, 2612–2621, <https://doi.org/10.1175/JAS-D-14-0319.1>.

860 Chen, Y.-C., Christensen, M. W., Stephens, G. L., and Seinfeld, J. H.: Satellite-based estimate of global
861 aerosol-cloud radiative forcing by marine warm clouds, *Nat. Geosci.*, 7, 643–646,
862 <https://doi.org/10.1038/ngeo2214>, 2014.

863 Christensen, M. W., Chen, Y.-C., and Stephens, G. L.: Aerosol indirect effect dictated by liquid clouds,
864 *J. Geophys. Res.*, 121, 14636-14650, <https://doi.org/10.1002/2016JD025245>, 2016.

865 Costantino, L. and Bréon, F. M.: Analysis of aerosol-cloud interaction from multi-sensor satellite
866 observations. *Geophys. Res. Lett.*, 37, L11801, doi:10.1029/2009GL041828, 2010.

867 Costantino, L. and Bréon, F. M.: Aerosol indirect effect on warm clouds over South-East Atlantic, from
868 co-located MODIS and CALIPSO observations, *Atmos. Chem. Phys.*, 13: 69-88, 2013.

869 Dagan, G., Yeheskel, N., Williams, A. I. L.: Radiative forcing from aerosol–cloud interactions enhanced
870 by large-scale circulation adjustments, *Nature geoscience*, 16, 1092-1098, 2023.

871 de Leeuw, G., R. van der A, J. Bai, Y. Xue, C. Varotsos, Z. Li, C. Fan, X. Chen, I. Christodoulakis, J.
872 Ding, X. Hou, G. Kouremadas, D. Li, J. Wang, M. Zara, K. Zhang, Y. Zhang.: Air Quality over China.
873 *Remote Sens.* 2021, 13, 3542. <https://doi.org/10.3390/rs13173542>, 2021.

874 de Leeuw, G., Fan, C, Li, Z., Dong, J., Li, Y., Ou, Y., and Zhu, S. (2022). Spatiotemporal variation and
875 provincial scale differences of the AOD across China during 2000–2021. *Atmospheric Pollution*
876 *Research* 13 (2022) 101359 (14 pp). <https://doi.org/10.1016/j.apr.2022.101359>.

877 de Leeuw, G., Kang, H., Fan, C., Li, Z., Fang, C., Zhang, Y. (2023). Meteorological and anthropogenic
878 contributions to changes in the Aerosol Optical Depth (AOD) over China during the last decade. *Atm.*
879 *Env.*, 301, 119676. <https://doi.org/10.1016/j.atmosenv.2023.119676>.

880 Ekman, A. M. L., Eva Nygren, Alejandro Baró Pérez, Matthias Schwarz, Gunilla Svensson, Nicolas
881 Bellouin.: Influence of horizontal resolution and complexity of aerosol–cloud interactions on marine
882 stratocumulus and stratocumulus-to-cumulus transition in HadGEM3-GC3.1, *Quart. J Royal Met Soc.*,
883 149, 755, 2049-2066, <https://doi.org/10.1002/qj.4494>, 2023.

884 Fan J, Wang Y, Rosenfeld D, et al.: Review of aerosol-cloud interactions: Mechanisms, significance, and
885 challenges. *Journal of the Atmospheric Sciences*,73(11): 4221-4252, 2016.

886 Fan, J., Zhang, Y., Li, Z., Yan, H., Prabhakaran, T., Rosenfeld, D., & Khain, A.: Unveiling aerosol
887 impacts on deep convective clouds: Scientific concept, modeling, observational analysis, and future
888 direction, *Journal of Geophysical Research: Atmospheres*, 130, e2024JD041931. <https://doi.org/10.1029/2024JD041931>, 2025.

890 Feingold, G., Remer, L. A., Ramaprasad, J., Kaufman, Y. J.: Analysis of smoke impact on clouds in
891 Brazilian biomass burning regions: an extension of Twomey’s approach, *J. Geophys. Res.*, 106 (D19),
892 22907-22922, 2001.

893 Feingold, G. Modeling of the first indirect effect: analysis of measurement requirements, *Geophys. Res.*
894 *Lett.*, 30, 1997, doi:10.1029/2003GL017967, 2003.

895 Feingold, G., Goren, T., and Yamaguchi, T.: Quantifying albedo susceptibility biases in shallow clouds,
896 *Atmos. Chem. Phys.*, 22, 3303–3319, <https://doi.org/10.5194/acp-22-3303-2022>, 2022.

897 Grandey, B.S., Stier, P.: A critical look at spatial scale choices in satellite-based aerosol indirect effect
898 studies. *Atmos. Chem. Phys.*, 10, 11459-11470, 2010.

899 Gryspeerdt, E., Stier, P., and Partridge, D. G.: Satellite observations of cloud regime development: the
900 role of aerosol processes, *Atmos. Chem. Phys.*, 14, 1141-1158, doi:10.5194/acp-14-1141-2014, 2014.

901 Gryspeerdt, E., Povey, A. C., Grainger, R. G., Hasekamp, O., Hsu, N. C., Mulcahy, J. P., Sayer, A. M.,
902 and Sorooshian, A.: Uncertainty in aerosol–cloud radiative forcing is driven by clean conditions, *Atmos.*
903 *Chem. Phys.*, 23, 4115–4122, <https://doi.org/10.5194/acp-23-4115-2023>, 2023.

904 Gryspeerdt, E., McCoy, D. T., Crosbie, E., Moore, R. H., Nott, G. J., Painemal, D., Small-Griswold, J.,
905 Sorooshian, A., and Ziemba, L.: The impact of sampling strategy on the cloud droplet number
906 concentration estimated from satellite data, *Atmos. Meas. Tech.*, 15, 3875–3892, 2022,
907 <https://doi.org/10.5194/amt-15-3875-2022>, 2022.

908 Glotfelty, T., Kiran Alapaty, Jian He, Patrick Hawbecker, Xiaoliang Song, and Guang Zhang. Studying
909 Scale Dependency of Aerosol–Cloud Interactions Using Multiscale Cloud Formulations, 77, 11, 2020.

910 Grosvenor, D. P., Sourdeval, O., Zuidema, P., Ackerman, A., Alexandrov, M. D., Bennartz, R., Boers,
911 R., Cairns, B., Chiu, J. C., Christensen, M., Deneke, H., Diamond, M., Feingold, G., Fridlind, A.,
912 Hünerbein, A., Knist, C., Kollias, P., Marshak, A., McCoy, D., Merk, D., Painemal, D., Rausch, J.,
913 Rosenfeld, D., Russchenberg, H., Seifert, P., Sinclair, K., Stier, P., Diedenhoven, B. V., Wendisch, M.,
914 Werner, F., Wood, R., Zhang, Z., and Quaas, J.: Remote sensing of droplet number concentration in
915 warm clouds: A review of the current state of knowledge and perspectives, *Rev. Geophys.*, 56, 409–453,
916 <https://doi.org/10.1029/2017RG000593>, 2018.

917 Han, X., Zhao, B., Lin, Y., Chen, Q., Shi, H., Jiang, Z., et al.: Type-dependent impact of aerosols on
918 precipitation associated with deep convective cloud over East Asia, *Journal of Geophysical Research:*
919 *Atmospheres*, 127, e2021JD036127. <https://doi.org/10.1029/2021JD036127>, 2022.

920 Hassan, T., Zhang, K., Li, J., Singh, B., Zhang, S., Wang, H., and Ma, P.: Impacts of spatial heterogeneity
921 of anthropogenic aerosol emissions in a regionally refined global aerosol–climate model, *Geosci. Model*
922 *Dev.*, 17, 3507–3532, 2024.

923 Huang, R. J., Zhang, Y. L., Bozzetti, C., et al. High secondary aerosol contribution to particulate pollution
924 during haze events in China, *Nature*, 514, 218–222, 2014.

925 Jia, H. L., Ma, X. Y., Quaas, J., Yin, Y., Qiu, T.: Is positive correlation between cloud droplet effective
926 radius and aerosol optical depth over land due to retrieval artifacts or real physical processes?
927 *Atmospheric Chemistry and Physics*, 19, 13, 8879–8896, 2019.

928 Jia, H., Quaas, J., Gryspeerdt, E., Böhm, C., & Sourdeval, O.: Addressing the difficulties in quantifying
929 droplet number response to aerosol from satellite observations, *Atmospheric Chemistry and Physics*,
930 22(11), 7353–7372. <https://doi.org/10.5194/acp-22-7353-2022>, 2022.

931 Jones, T. A., Christopher, S. A., & Quaas, J.: A six year satellite-based assessment of the regional
932 variations in aerosol indirect effects. *Atmospheric Chemistry and Physics*, 9, 4091, 2009.

933 Koren, I., Kaufman, Y. J., Rosenfeld, D., Remer, L. A., Rudich, Y.: Aerosol invigoration and
934 restructuring of Atlantic convective clouds. *Geophys. Res. Lett.*, 32 (14), L14828, 2005.

935 Kaufman, Y.J. and Fraser, R.S.: The effect of smoke particles on clouds and climate forcing. *Science*,
936 1997. 277(5332): p. 1636-1639.

937 Kaufman, Y. J., Remer, L., Tanré, D., Li, R., Kleidman, R., Mattoo, S., Levy, R., Eck, T., Holben, B.,
938 Ichoku, C., Martins, J., and Koren, I.: A critical examination of the residual cloud contamination and
939 diurnal sampling effects on MODIS estimates of aerosol over ocean, *IEEE Trans. Geosci. Remote Sens.*,
940 43, 2886–2897, 2005.

941 Kaufman, Y.J., Remer, L.A., Tanré, D., Li, R.R., Kleidman, R., Mattoo, S., Levy, R.C., Eck, T.F., Holben,
942 B.N., Ichoku, C., Member, IEEE, Martins, J.V., and Koren, I.: A Critical Examination of the Residual
943 Cloud Contamination and Diurnal Sampling Effects on MODIS Estimates of Aerosol Over Ocean, *IEEE*
944 *TRANSACTIONS ON GEOSCIENCE AND REMOTE SENSING*, 43, 12, 2005.

945 Kim, S. W., S. C. Yoon, J. Y. Kim, and S. Y. Kim (2007), Seasonal and monthly variations of columnar
946 aerosol optical properties over East Asia determined from multi-year MODIS, LIDAR, and AERONET
947 Sun/sky radiometer measurements, *Atmos. Environ.*, 41(8), 1634–1651,
948 doi:10.1016/j.atmosenv.2006.10.044.

949 King, M. D., Tsay, S. C., Platnick, S. E., Wang, M., and Liou, K. N.: Cloud Retrieval Algorithms for
950 MODIS: Optical Thickness, Effective Particle Radius, and Thermodynamic Phase, MODIS Algorithm
951 Theoretical Basis Document, available at: http://eosps.nasa.gov/sites/default/files/atbd/atbd_mod05.pdf,
952 1997.

953 King, M. D., Menzel, W. P., Kaufman, Y. J., Tanré, D., Gao, B. C., Platnick, S., Ackerman, S. A., Remer,
954 L. A., Pincus, R., and Hubanks, P. A.: Cloud and aerosol properties, precipitable water, and profiles of
955 temperature and water vapor from MODIS, *IEEE T. Geosci. Remote*, 41, 442–458,
956 doi:10.1109/TGRS.2002.808226, 2003.

957 Lebsock, M., Morrison, H., Gettelman, A.: Microphysical implications of cloud-precipitation covariance
958 derived from satellite remote sensing. *Journal of Geophysical Research: Atmosphere*, 118, 6521-6533,
959 2013.

960 Levy, R. C., Mattoo, S., Munchak, L. A., Remer, L. A., Sayer, A. M., Patadia, F., and Hsu, N. C.: The
961 Collection 6 MODIS aerosol products over land and ocean, *Atmos. Meas. Tech.*, 6, 2989-3034,
962 <https://doi.org/10.5194/amt-6-2989-2013>, 2013.

963 Levy, R. C., Remer, L. A., Kleidman, R. G., Mattoo, S., Ichoku, C., Kahn, R., and Eck, T. F.: Global
964 evaluation of the Collection 5 MODIS dark-target aerosol products over land, *Atmos. Chem. Phys.*, 10,
965 10399–10420, doi:10.5194/acp-10-10399-2010, 2010.

966 Lee, S. S., Donner, L. J., Phillips, V. T. J. Impacts of aerosol chemical composition on microphysics and
967 precipitation in deep convection, *Atmospheric Research*, 94, 220–237, 2009.

968 Lee, H.-H., Zheng, X., Qiu, S., and Wang, Y.: Numerical case study of the aerosol–cloud interactions in
969 warm boundary layer clouds over the eastern North Atlantic with an interactive chemistry module, *Atmos.*
970 *Chem. Phys.*, 25, 6069–6091, <https://doi.org/10.5194/acp-25-6069-2025>, 2025.

971 Leung, G. R., Saleeby, S. M., Sokolowsky, G. A., Freeman, S. W., and van den Heever, S. C.: Aerosol–
972 cloud impacts on aerosol detrainment and rainout in shallow maritime tropical clouds, *Atmos. Chem.*
973 *Phys.*, 23, 5263–5278, <https://doi.org/10.5194/acp-23-5263-2023>, 2023.

974 Li, G. H., Wang, Y., Zhang, R. Y.: Implementation of a two-moment bulk microphysics scheme to the
975 WRF model to investigate aerosol-cloud interaction, *Journal of Geophysical Research-Atmospheres*, 113,
976 D15, <https://doi.org/10.1029/2007JD009361>, 2008.

977 Li, Z., et al.: Aerosol and monsoon climate interactions over Asia, *Rev. Geophys.*, 54, 866–929,
978 doi:10.1002/2015RG000500, 2016.

979 Li, Y., Liu, X., and Cai, H.: Numerical simulation of aerosol concentration effects on cloud droplet size
980 spectrum evolutions of warm stratiform clouds in Jiangxi, China, *Atmos. Chem. Phys.*, 24, 13525–13540,
981 <https://doi.org/10.5194/acp-24-13525-2024>, 2024.

982 Liu, Y., Lin, T., Zhang, J., Wang, F., Huang, Y., Wu, X., Ye, H., Zhang, G., Cao, X., and de Leeuw, G.:
983 Opposite effects of aerosols and meteorological parameters on warm clouds in two contrasting regions
984 over eastern China, *Atmos. Chem. Phys.*, 24, 4651–4673, <https://doi.org/10.5194/acp-24-4651-2024>,
985 2024.

986 Liu, Q., Duan, S. Y., He, Q. S., Chen, Y. H., Zhang, H., Cheng, N. X., Huang, Y. W., Chen, B., Zhan, Q.
987 Y., Li, J. Z.: The variability of warm cloud droplet radius induced by aerosols and water vapor in
988 Shanghai from MODIS observations, *Atmospheric Research*, 253, 105470, 2021.

989 Liu, Q., Shen, X., Li, L., et al. Impacts of Aerosol Chemical Composition on Cloud Condensation Nuclei
990 (CCN) Activity during Wintertime in Beijing, China. *Remote Sens.*, 15, 4119, 2023.

991 Liu, T. Q., Liu, Q., Chen, Y. H., Wang, W. C., Zhang, H., Li, D., Sheng, J.: Effect of aerosols on the
992 macro- and micro-physical properties of warm clouds in the Beijing-Tianjin-Hebei region. *Science of
993 the Total Environment*, 720, 137618, 2020.

994 Liu, Y., Zhang, J., Zhou, P., Lin, T., Hong, J., Shi, L., Yao, F., Wu, J., Guo, H., and de Leeuw, G.:
995 Satellite-based estimate of the variability of warm cloud properties associated with aerosol and
996 meteorological conditions, *Atmos. Chem. Phys.*, 18, 18187-18202, [https://doi.org/10.5194/acp-18-](https://doi.org/10.5194/acp-18-18187-2018)
997 18187-2018, 2018.

998 Liu, Y., de Leeuw, G., Kerminen, V.-M., Zhang, J., Zhou, P., Nie, W., Qi, X., Hong, J., Wang, Y., Ding,
999 A., Guo, H., Krüger, O., Kulmala, M., and Petäjä, T.: Analysis of aerosol effects on warm clouds over
1000 the Yangtze River Delta from multi-sensor satellite observations, *Atmos. Chem. Phys.*, 17, 5623-5641,
1001 <https://doi.org/10.5194/acp-17-5623-2017>, 2017.

1002 Liu, Z., Vaughan, M., Winker, D., Kittaka, C., Getzewich, B., Kuehn, R., Omar, A., Powell, K., Trepte,
1003 C., and Hostetler, C.: The CALIPSO lidar cloud and aerosol discrimination: Version 2 algorithm and
1004 initial assessment of performance, *J. Atmos. Ocean. Tech.*, 26, 1198–1213, 2009.

1005 Ma, X., Jia, H., Yu, F., and Quaas, J.: Opposite aerosol index-cloud droplet effective radius correlations
1006 over major industrial regions and their adjacent oceans, *Geophys. Res. Lett.*, 45, 5771–5778,
1007 <https://doi.org/10.1029/2018GL077562>, 2018.

1008 Ma, P.-L., P. J. Rasch, M. Wang, H. Wang, S. J. Ghan, R. C. Easter, W. I. Gustafson Jr., X. Liu, Y.
1009 Zhang, and H.-Y. Ma (2015), How does increasing horizontal resolution in a global climate model
1010 improve the simulation of aerosol-cloud interactions?, *Geophys. Res. Lett.*, 42, 5058–5065,
1011 [doi:10.1002/2015GL064183](https://doi.org/10.1002/2015GL064183).

1012 Marchant, B., et al.: MODIS Collection 6 shortwave-derived cloud phase classification algorithm and
1013 comparisons with CALIOP, *Atmos. Meas. Tech. Discuss.*, 8, 11893–11924, 2015.

1014 Matheson, M. A., Coakley Jr., J. A., and Tahnk, W. R.: Aerosol and cloud property from relationships
1015 for summer stratiform clouds in the northeastern Atlantic from advanced very high resolution radiometer
1016 observations, *J. Geophys. Res.*, 110, D24204, doi:10.1029/2005JD006165, 2005.

1017 McComiskey, A., & Feingold, G: The scale problem in quantifying aerosol indirect effects. *Atmospheric*
1018 *Chemistry and Physics*, 12, 1031. <https://doi.org/10.5194/acp-12-1031-2012>, 2012.

1019 Meskhidze, N., Nenes, A.: Effects of ocean ecosystem on marine aerosol-cloud interaction. *Adv.*
1020 *Meteorol*, doi:10.1155/2010/239808, 2010.

1021 Mohebalhojeh, M., Frederick, S., Riemer, N., & West, M. (2026). A Metric for Quantifying Spatial
1022 Heterogeneity in Gridded Atmospheric Fields. *Earth and Space Science* (preprint).

1023 Murray-Watson, R. J. and Gryspeerdt, E.: Stability-dependent increases in liquid water with droplet
1024 number in the Arctic, *Atmos. Chem. Phys.*, 22, 5743–5756, <https://doi.org/10.5194/acp-22-5743-2022>,
1025 2022.

1026 McComiskey, A., G. Feingold, A. S. Frisch, D. D. Turner, M. A. Miller, J. C. Chiu, Q. Min, and J. A.
1027 Ogren (2009), Anassessment of aerosol-cloud interactions in marine stratus clouds based on surface
1028 remote sensing, *J. Geophys. Res.*, 114, D09203,doi:10.1029/2008JD011006.

1029 Platnick, S., et al., MODIS Cloud optical properties: User guide for the Collection 6/6.1 level-2
1030 MOD06/MYD06 product and associated level-3 data sets. v1.1, July 2018.

1031 Proestakis, E., Amiridis, V., Marinou, E., Georgoulas, A. K., Solomos, S., Kazadzis, S., Chimot, J., Che,
1032 H., Alexandri, G., Binietoglou, I., Daskalopoulou, V., Kourtidis, K. A., de Leeuw, G., and van der A, R.
1033 J.: Nine-year spatial and temporal evolution of desert dust aerosols over South and East Asia as revealed
1034 by CALIOP, *Atmos. Chem. Phys.*, 18, 1337-1362, <https://doi.org/10.5194/acp-18-1337-2018>, 2018.

1035 Possner A., Zubler, E. M., Lohmann, U., and Schär, C.: The resolution dependence of cloud effects
1036 and ship-induced aerosol-cloud interactions in marine stratocumulus, *J. Geophys. Res. Atmos.*, 121,
1037 4810–4829, doi:10.1002/2015JD024685, 2016.

1038 Pandey, S. K., Vinoj, V., Panwar, A.: The short-term variability of aerosols and their impact on cloud
1039 properties and radiative effect over the Indo-Gangetic Plain. *Atmospheric Pollution Research*, 11, 630-
1040 638, 2020.

1041 Platnick, S., Meyer, K. G., King, M. D., Wind, G., Amarasinghe, N., Marchant, B., Arnold, G. T., Zhang,
1042 Z., Hubanks, P. A., Holz, R. E., Yang, P., Ridgway, W. L., Riedi, J.: The MODIS cloud optical and

1043 microphysical products: Collection 6 updates and examples from Terra and Aqua. *IEEE Trans Geosci*
1044 *Remote Sens.* Jan;55(1):502-525. doi: 10.1109/TGRS.2016.2610522, 2017.

1045 Quaas, J., Boucher, O., Bellouin, N., Kinne, S.: Satellite-based estimate of the direct and indirect aerosol
1046 climate forcing, *J. Geophys. Res.*, 113, D05204, doi:10.1029/2007JD008962, 2008.

1047 Quaas, J., Stevens, B., Stier, P., and Lohmann, U.: Interpreting the cloud cover – aerosol optical depth
1048 relationship found in satellite data using a general circulation model, *Atmos. Chem. Phys.*, 10, 6129-
1049 6135, <https://doi.org/10.5194/acp-10-6129-2010>, 2010.

1050 Quaas, J., Boucher, O., and Lohmann, U.: Constraining the total aerosol indirect effect in the LMDZ and
1051 ECHAM4 GCMs using MODIS satellite data, *Atmos. Chem. Phys.*, 6, 947–955,
1052 <https://doi.org/10.5194/acp-6-947-2006>, 2006.

1053 Quaas, J., Ming, Y., Menon, S., Takemura, T., Wang, M., Penner, J. E., Gettelman, A., Lohmann, U.,
1054 Bellouin, N., Boucher, O., Sayer, A. M., Thomas, G. E., McComiskey, A., Feingold, G., Hoose, C.,
1055 Kristjánsson, J. E., Liu, X., Balkanski, Y., Donner, L. J., Ginoux, P. A., Stier, P., Grandey, B., Feichter,
1056 J., Sednev, I., Bauer, S. E., Koch, D., Grainger, R. G., Kirkevåg, A., Iversen, T., Seland, Ø., Easter, R.,
1057 Ghan, S. J., Rasch, P. J., Morrison, H., Lamarque, J.-F., Iacono, M. J., Kinne, S., and Schulz, M.: Aerosol
1058 indirect effects – general circulation model intercomparison and evaluation with satellite data, *Atmos.*
1059 *Chem. Phys.*, 9, 8697–8717, <https://doi.org/10.5194/acp-9-8697-2009>, 2009.

1060 Rao, S., Dey, S.: Consistent signal of aerosol indirect and semi-direct effect on water clouds in the
1061 oceanic regions adjacent to the Indian subcontinent. *Atmospheric Research*, 232, 2020.

1062 Remer, L. A., Kaufman, Y. J., Tanre, D., Mattoo, S., Chu, D. A., Martins, J. V., Li, R. R., Ichoku, C.,
1063 Levy, R. C., Kleidman, R. G., Eck, T. F., Vermote, E., and Holben, B. N.: The MODIS aerosol algorithm,
1064 products, and validation, *J. Atmos. Sci.*, 62, 947–973, <https://doi.org/10.1175/JAS3385.1>, 2005.

1065 Rosenfeld, D., Zhu, Y. N., Wang, M. H., Zheng, Y. T., Goren, T., Yu, S. C.: Aerosol-driven droplet
1066 concentrations dominate coverage and water of oceanic low-level clouds, *Science*, 363, 6427, 2019.

1067 Sarna, K. and Russchenberg, H. W. J.: Ground-based remote sensing scheme for monitoring aerosol–
1068 cloud interactions, *Atmos. Meas. Tech.*, 9, 1039–1050, <https://doi.org/10.5194/amt-9-1039-2016>, 2016.

1069 Saponaro, G., Kolmonen, P., Sogacheva, L., Rodriguez, E., Virtanen, T., de Leeus, G.: Estimates of the
1070 aerosol indirect effect over the Baltic Sea region derived from 12 years of MODIS observations, *Atmos.*
1071 *Chem. Phys.*, 17, 3133-3143, 2017.

1072 Stephens, G., Vane, D. G., Boain, R. J., Mace, G. G., Sassen, K., Wang, Z., Illingworth, A. J., O'Connor,
1073 E. J., Rossow, W. B., Durden, S. L., Miller, S. D., Austin, R. T., Benedetti, A., and Mitrescu, C.: The
1074 CloudSat Science Team: The CloudSat mission and the A-Train, *B. Am. Meteorol. Soc.*, 83, 1771–1790,
1075 2002.

1076 Sourdeval, O., Laurent C.-Labonnote, Anthony J. Baran, Johannes Mülmenstädt, Gérard Brogniez.: A
1077 methodology for simultaneous retrieval of ice and liquid water cloud properties. Part 2: Near-global
1078 retrievals and evaluation against A-Train products, *Quarterly Journal of the Royal Meteorological*
1079 *Society*, 142, 701, 3063-3081, 2016.

1080 Sundström, A.-M., Kolmonen, P., Sogacheva, L., and de Leeuw, D.: Aerosol retrievals over China with
1081 the AATSR dual view algorithm, *Remote Sens. Environ.*, 116, 189–198, 2012.

1082 Theodore L. Anderson, Robert J. Charlson, David M. Winker, John A. Ogren, and Kim Holmén.:
1083 Mesoscale Variations of Tropospheric Aerosols, *Journal of the Atmospheric Sciences*, 60, 1,
1084 [https://doi.org/10.1175/1520-0469\(2003\)060<0119:MVOTA>2.0.CO;2](https://doi.org/10.1175/1520-0469(2003)060<0119:MVOTA>2.0.CO;2), 2003.

1085 Tang, J., Wang, P., Mickley, L. J., Xia, X., Liao, H., Yue, X., et al.: Positive relationship between liquid
1086 cloud droplet effective radius and aerosol optical depth over Eastern China from satellite data.
1087 *Atmospheric Environment*, 84, 244-253. <https://doi.org/10.1016/j.atmosenv.2013.08.024>, 2014.

1088 Tao, W. K., Chen, J. P., Li, Z., Wang, C. E., Zhang, C. D.: Impact of aerosols on convective clouds and
1089 precipitation, *Reviews of Geophysics*, 50(2), 2012.

1090 Twomey, S. Pollution and the planetary albedo, *Atmos. Environ.*, 1974, 41, 120-125.

1091 Twomey, S.: The influence of pollution on the shortwave albedo of clouds, *J. Atmos. Sci.* 34(7), 1149-
1092 1152, 1977.

1093 Wang, F., Guo, J., Zhang, J., Wu, Y., Zhang, X., Deng, M., and Li, X.: Satellite observed aerosol-induced
1094 variability in warm cloud properties under different meteorological conditions over eastern China, *Atmos.*
1095 *Environ.*, 84, 122–132, 2014.

1096 Wang, F., Guo, J., Zhang, J., Wu, Y., Zhang, X., Deng, M., Li, X.: Satellite observed aerosol-induced
1097 variability in warm cloud properties under different meteorological conditions over eastern China, *Atmos.*
1098 *Environ.*, 84, 122-132, 2014.

1099 Wang, Y., Wang, Y., Song, X., Shang, Y., Zhou, Y., Huang, X., Li, Z.: The impact of particulate pollution
1100 control on aerosol hygroscopicity and CCN activity in North China, *Environmental Research Letters*, 18,
1101 074028, 2023.

1102 Winker, D. M., Pelon, J. R., and McCormick, M. P.: The CALIPSO mission: Spaceborne lidar for
1103 observation of aerosols and clouds, *Proc. SPIE, Lidar Remote Sensing for Industry and Environment*
1104 *Monitoring III*, 4893, doi:10.1117/12.466539, 2003.

1105 Winker, D. M., Hunt, W. H., and McGill, M. J.: Initial performance assessment of CALIOP, *Geophys.*
1106 *Res. Lett.*, 34, L19803, doi:10.1029/2007GL030135, 2007.

1107 Winker, D. M., Vaughan, M. A., Omar, A., Hu, Y., Powell, K. A., Liu, Z. Y., Hunt, W. H., Young, S.
1108 A.: Overview of the CALIPSO Mission and CALIOP Data Processing Algorithms, *Journal of*
1109 *Atmospheric and Oceanic Technology*, 26 (11), 2310-2323, 2009. doi:10.1175/2009JTECHA1281.1.

1110 Winker, D. M., Pelon, J., Coakley Jr, J. A., Ackerman, S. A., Charlson, R. J., Colarco, P. R., Flamant, P.,
1111 Fu, Q., Hoff, R. M., Kittaka, C., Kubar, T. L., Le Treut, H., McCormick, M. P., Mégie, G., Poole, L.,
1112 Powell, K., Trepte, C., Vaughan, M. A., and Wielicki, B. A.: The CALIPSO Mission. *Bulletin of*
1113 *American Meteorological Society*, 91(9), 1211-1230, 2010.

1114 Wang, F., Guo, J., Zhang, J., Huang, J., Min, M., Chen, T., Liu, H., Deng, M., Li, X.: Multi-sensor
1115 quantification of aerosol-induced variability in warm clouds over eastern China, *Atmos. Environ.*, 113:
1116 1-9, 2015. <http://dx.doi.org/10.1016/j.atmosenv.2015.04.063>.

1117 Yuan, T., Li, Z., Zhang, R., and Fan, J.: Increase of cloud droplet size with aerosol optical depth: an
1118 observation and modeling study, *J. Geophys. Res.*, 113, D04201, doi:10.1029/2007JD008632, 2008.

1119 Zhang, L., Li, J., Li, J., Li, R., Zhang, W., Lei, M., et al.: Studying the impacts of meteorological factors
1120 on distribution of cloud horizontal scales based on active satellite, *Journal of Geophysical Research:*
1121 *Atmospheres*, 129, e2024JD041844, <https://doi.org/10.1029/2024JD041844>, 2024.

1122 Zhang, Q., Meng, J., Quan, J., et al. Impact of aerosol composition on cloud condensation nuclei activity,
1123 *Atmos. Chem. Phys.*, 12, 3783–3790, 2012.

1124 Zhao, J., Ma, X., Quaas, J., and Yang, T.: How meteorological conditions influence aerosol-cloud
1125 interactions under different pollution regimes, *Atmos. Chem. Phys.*, 25, 17701–17723,
1126 <https://doi.org/10.5194/acp-25-17701-2025>, 2025.

1127 Zheng, B., Tong, D., Li, M., Liu, F., Hong, C., Geng, G., Li, H., Li, X., Peng, L., Qi, J., Yan, L., Zhang,
1128 Y., Zhao, H., Zheng, Y., He, K., and Zhang, Q.: Trends in China's anthropogenic emissions since 2010
1129 as the consequence of clean air actions, *Atmos. Chem. Phys.*, 18, 14095–14111,
1130 <https://doi.org/10.5194/acp-18-14095-2018>, 2018.

1131 Zheng, X., Dong, X., Xi, B., Logan, T., and Wang, Y.: Distinctive aerosol–cloud–precipitation
1132 interactions in marine boundary layer clouds from the ACE-ENA and SOCRATES aircraft field
1133 campaigns, *Atmos. Chem. Phys.*, 24, 10323–10347, <https://doi.org/10.5194/acp-24-10323-2024>, 2024.

1134 Zheng, X., Xi, B., Dong, X., Logan, T., Wang, Y., and Wu, P.: Investigation of aerosol–cloud interactions
1135 under different absorptive aerosol regimes using Atmospheric Radiation Measurement (ARM) southern
1136 Great Plains (SGP) ground-based measurements, *Atmos. Chem. Phys.*, 20, 3483–3501,
1137 <https://doi.org/10.5194/acp-20-3483-2020>, 2020.

1138

1139

1140

1141